Journal of Positive Sciences (JPS) eISSN: 2582-9351, https://positive-sciences.com JPS. 2026 Oct; 6(6): 67-102

Article info
Received on: 09.09.2026
Accepted on: 10.10.2026
Published on: 21.11.2026
doi: https://doi.org/10.52688/JPS267390

Research Article

Powder-Metallurgy Al–3Mg–1Zn/ZrB_2–CeO_2 Hybrid Composites: Microstructural Evolution, Mechanical Integrity, and Tafel Polarization Response

Hussein Mousa Habeeb [1], Mohammed RASHEED [2,*]

[1] Department of Mechanical Engineering, College of Engineering, University of Kufa, Najaf, Iraq.
[2] College of Production Engineering & Metallurgy, University of Technology- Iraq, Baghdad, Iraq

[*] rasheed.mohammed40@yahoo.com

ABSTRACT

This research investigates the microstructure evolution, phase composition, densification behavior, mechanical integrity and electrochemical response of powder metallurgy Al–3Mg–1Zn hybrid composites strengthened with 0–4 wt.% ZrB_2–CeO_2 at a fixed mass ratio of 3:1. The relationships between the reinforcement content, the microstructural features and the performance of the composite are investigated on five mixtures named AMC0-4. The particle distribution, grain morphology, crystallographic features and phase composition are examined by optical microscopy, field-emission scanning electron microscopy combined with energy-dispersive X-ray spectroscopy (FESEM–EDS), electron backscatter diffraction (EBSD) and X-ray diffraction (XRD). Densification, residual porosity and internal defects are examined using Archimedes density measurements and micro-computed tomography. The mechanical integrity is evaluated by Vickers hardness, nanoindentation, tensile and compression tests. The electrochemical behavior is evaluated by open-circuit potential (OCP) monitoring and potentiodynamic polarization. The tests show that AMC3 is a good material. It has a relative density of 96.2%, an apparent porosity of 3.8%, a Vickers hardness of 119 HV0.5, an indentation hardness of 1.40 GPa, an ultimate tensile strength of 350 MPa, a peak compressive strength of 439 MPa and an elongation of 12.0%. The corresponding measured electrochemical values comprise a corrosion current density of 1.9×10^{-7} A.cm^{-2} and an OCP of approximately −0.523 V versus Ag/AgCl. These experimentaly numerical trends indicate a potentially favorable balance between densification, reinforcement strengthening, ductility, and electrochemical stability at intermediate ceramic loading. This study puts forward a framework for integration of characterization to investigate the interrelations between composition, microstructure and properties. The aluminum based hybrid composites are found to be promising for the structural engineering.

KEYWORDS: Powder metallurgy; Al–Mg–Zn alloy; ZrB_2/CeO_2 hybrid reinforcement; EBSD; Micro-CT; Nanoindentation; Tensile strength; Open-circuit potential; Tafel polarization; Corrosion current density

INTRODUCTION

Light Al-based structures need to be of low densities that can reliably respond to deformation, stretching and squeezing. Mg and Zn can influence the secondary phase composition, oxidation and solid-solution strengthening in Al–3Mg–1Zn, and direct characterization is necessary to understand how they remain in place and where they are located after sintering. The reinforcement of ZrB_2 –CeO_2 matrices is provided by their consolidation and their interfacial bonding with other materials, and not only by the ceramic loading [1].

*Corresponding author
Mohammed RASHEED,
College of Production Engineering & Metallurgy, University of Technology- Iraq, Baghdad, Iraq
e-mail: rasheed.mohammed40@yahoo.com

Powder metallurgy allows for controlled mixing and relatively low temperature consolidation but also unknowns in powder size, native oxide films, milling-induced morphology, compaction history and residual interconnected porosity. Polished microscopy, EBSD, Archimedes measurements and 3D tomography are not substitutes, but methods that work hand-in-hand to distinguish processing effects from reinforcement effects [2, 3].

If well bonded to the matrix, ZrB_2 can transfer load and stop the dislocation movement. In contrast, CeO_2 can modify the oxide/interfacial environment or form a separate phase after sintering. Co-addition does not by itself prove chemical or mechanical synergy, so ZrB_2-only and CeO_2-only matched controls would have to be used for certainty, with accurate XRD/EDS identification of the resulting phases [4, 5].

A major methodological problem is to separate the effect of the content of the reinforcement from the effect of the quality of the consolidation. Two compacts with the same nominal ceramic fraction can have different properties if they differ in oxide film continuity, pore topology or local particle clustering. Thus, density normalized comparisons, phase aware microscopy and separate processing of batches are required to distinguish a true ceramic response from a fabrication artifact. If you compare things only based on their highest hardness or tensile strength you could miss failures caused by flaws and differences between samples [5].

For the electrochemical part, we need the same exposed area, the same electrolyte chemistry, the same surface preparation, the same reference electrode scale and the same polarization protocol for each composition to understand. Just shifting the open circuit potential to higher positive potentials is not enough to obtain a lower degradation rate. The fitted corrosion current densities are affected by localized attack and by the appropriateness of the selected Tafel regions. For relating polarization and microstructure we have to think about the specimen history and the outcome of the test and not just to blame the nominal ZrB_2-CeO_2 ratio [1].

The main question is whether a ceramic intermediate fraction can add more strength and stability to the material and at the same time reduce its susceptibility to chloride damage. Vickers and nanoindentation are at different levels of contact, tension and compression are at different levels of stress and the responses don't have to get better at the same time [6].

We filled a large gap in our knowledge by investigating the relationships between the placement of ceramic reinforcements, the phase makeup, residual porosity, the mechanical reliability, and the electrochemical polarization mechanism in powder metallurgy produced Al–3Mg–1Zn/(ZrB_2–CeO_2) hybrid composites. We study five different compositions (AMC0–AMC4) using a suite of tools including optical microscopy, FESEM–EDS, EBSD, XRD, density and porosity analysis, micro-computed tomography, Vickers hardness, nanoindentation, tensile and compressive testing, and electrochemical polarization analysis. This comprehensive strategy is intended to define quantitative relationships between the amount of reinforcement, the evolution of the microstructure, the mechanical performances of the material and its behavior in the face of corrosion. We're searching for the best reinforcement composition in terms of densification, mechanical strength and electrochemical stability. We're also looking at the effects of particle agglomeration and microstructural heterogeneity at higher concentrations of ceramics. A systematic approach to study structure–property relationships and to understand the functioning of these hybrid metal–ceramic composites is given by the combination of complementary characterization techniques [4].

MATERIALS AND EXPERIMENTAL PROCEDURES

COMPOSITION SELECTION AND POWDER-METALLURGY ROUTE

We prepared five hybrid composites from Al, 3Mg and 1Zn. They are named AMC0, AMC1, AMC2, AMC3 and AMC4. We prepared them by powder metallurgy and wanted to observe the effect of the reinforcement content ZrB_2 –CeO_2 on their microstructural, mechanical and electrochemical properties. This was achieved by varying the ceramic reinforcement from 0 to 4% in steps of 1% with the ZrB_2:CeO_2 mass ratio fixed at 3:1. The metallic part was an alloy of Al, 3Mg and 1Zn, the masses of the different parts being

*Corresponding author
Mohammed RASHEED,
College of Production Engineering & Metallurgy, University of Technology- Iraq, Baghdad, Iraq
e-mail: rasheed.mohammed40@yahoo.com

varied proportionally to the increasing ceramic content. Table 1 shows the major chemicals that comprised the five formulations that were prepared. Figure 1 is a simplified flowchart showing the processing steps for powder metallurgy: weighing of the powder, mixing, compacting, sintering and preparation of the specimen.

The starting powders were selected based on their chemical purity, particle size and their suitability for powder-metallurgy processing. After the compositions were fixed, the powder batches were weighted and mixed to guaranty an even distribution of the ZrB_2 and CeO_2 reinforcements in the aluminum-based matrix. Much attention was paid to control particle segregation, agglomeration and possible contamination during handling and processing of powder. After the preparation of powder mixtures, they were pressed so that they could obtain specimens for testing their microstructure, strength and electrical conductivity [2].



Fig. 1. Schematic illustration of the powder metallurgy process for the fabrication of Al–3Mg–1Zn/ZrB_2–CeO_2 hybrid composites.

Table 1. The chemical compositions (in weight percentage) of the five hybrid composites (AMC0–AMC4).

Code	Al	Mg	Zn	ZrB_2	CeO_2
AMC0	96.00	3.00	1.00	0	0
AMC1	95.04	2.97	0.99	0.75	0.25
AMC2	94.08	2.94	0.98	1.50	0.50
AMC3	93.12	2.91	0.97	2.25	0.75
AMC4	92.16	2.88	0.96	3.00	1.00
AMZ3	93.12	2.91	0.97	3.00	0
AMC3C	93.12	2.91	0.97	0	3.00

The constituent powders were homogenized through a wet-assisted mechanical milling process using ethanol as the milling medium. The milling procedure was conducted for 4 h at a rotational speed of 200 rpm, with a ball-to-powder mass ratio of 10:1. Following milling, the powder mixtures were dried under controlled conditions to remove residual ethanol before subsequent compaction and sintering. The milling parameters were selected to help in uniform distribution of ZrB_2 and CeO_2 particles in the Al–3Mg–1Zn metal matrix and to minimize the possibility of particle aggregation and chemical contamination. The powder mixtures were homogenized and then prepared for consolidation and further information. Materials processing was carried out according to well-known rules of powder metallurgy for the fabrication of particle reinforced aluminum-matrix composites [3].

The compositions of the five fabricated composites (AMC0–AMC4) were designed with a total mass fraction of 100 wt.% for each formulation. The Al-3Mg-1Zn metallic fraction decreased in the same ratio with increasing combined ZrB_2-CeO_2 reinforcement amount from 0 to 4 wt.%. However, the Mg and Zn concentrations in the alloy matrix were constant. The mass fraction of Mg and Zn slightly decreased with the increase of the reinforcement content, but the ratio of Mg and Zn was maintained. In all the reinforced mixtures the mass ratio of ZrB_2 to CeO_2 was 3:1. This compositional design allowed to test the effect of ceramics addition in a planned manner, while keeping the normal chemistry of the metal fraction. Calculated chemical compositions are presented in Table 1 [1].

MATERIALS AND REAGENTS

The metallic matrix was made of aluminum (Al), magnesium (Mg) and zinc (Zn) powders. Zirconium diboride (ZrB_2) and cerium(IV) oxide (CeO_2) were used as hybrid ceramic reinforcements. For the

*Corresponding author
Mohammed RASHEED,
College of Production Engineering & Metallurgy, University of Technology- Iraq, Baghdad, Iraq
e-mail: rasheed.mohammed40@yahoo.com

electrochemical tests, sodium chloride (NaCl) was used as the chloride-containing electrolyte and ethanol (C_2H_6O) was used as the milling medium in the wet-assisted mechanical homogenization. The powders that make up the components were weighed in accordance with their known compositions from AMC0 to AMC4, while the mass ratio of ZrB_2:CeO_2 was maintained at 3:1 as shown in Table 1 [2].

The metallic matrix was prepared using aluminum powder (Al; molar mass 26.98 $g.mol^{-1}$), magnesium powder (Mg; 24.31 $g.mol^{-1}$), and zinc powder (Zn; 65.39 $g.mol^{-1}$). Aluminum powder with a purity of ≥99.95% and particle size below 75 μm (Sigma-Aldrich/Merck, product No. 202584), magnesium powder with a purity of ≥99.0% and particle-size grade of −50 mesh (Sigma-Aldrich/Merck, product No. 253987), and zinc powder with a purity of 99.995% and particle size below 150 μm (Sigma-Aldrich/Merck, product No. 324930) were used as the starting metallic powders. The powders were weighed in accordance with the nominal alloy compositions before incorporation of the ceramic reinforcements.

The hybrid reinforcement system comprised zirconium diboride (ZrB_2; molar mass 112.84 $g.mol^{-1}$) and cerium(IV) oxide (CeO_2; molar mass 172.11 $g.mol^{-1}$). ZrB_2 powder with a purity of ≥99.0% was used as the primary ceramic reinforcement, while CeO_2 nanopowder with a purity of 99.95% (trace rare-earth-metal basis) and nominal particle size below 50 nm (Sigma-Aldrich/Merck, product No. 700290) was incorporated as the secondary ceramic phase. The two ceramic powders were combined at a fixed ZrB_2:CeO_2 mass ratio of 3:1 and introduced into the Al–3Mg–1Zn metallic powder mixture according to the designed reinforcement concentrations.

Sodium chloride (NaCl; molar mass 58.44 $g.mol^{-1}$) with a purity of ≥99.5% (Sigma-Aldrich/Merck, product No. S7653) was used to prepare the aqueous chloride electrolyte employed in the electrochemical experiments. Ethanol (C_2H_6O; molar mass 46.07 $g.mol^{-1}$) with a purity of ≥99.8% was employed as the processing solvent during wet-assisted mechanical milling. The ethanol-assisted homogenization was performed for 4 h at a rotational speed of 200 rpm, using a ball-to-powder mass ratio of 10:1. Following milling, the powder mixtures were dried to remove the residual solvent before the subsequent consolidation stages. These processing conditions were maintained throughout the preparation of the five composite formulations [4].

COMPACTION, SINTERING, AND METALLOGRAPHIC PREPARATION

The mixed Al-3Mg-1Zn/ZrB-CeO powders were uniaxially cold compacted at a pressure of 400 MPa in a cylindrical steel die with an inner diameter of 8 mm. A dwell time of 60 s was maintained during the compaction process to improve the powder movement, increase the contact between particles and make the green compact more uniform. The samples in the shape of a cylinder were gently pushed out of the die after pressing to avoid cracking at the edges and mechanical damage. The weights and sizes of the green specimens were noted to find the density and to see whether the size is consistent over the five compositions (AMC0–AMC4). Samples to be mechanically tested were prepared according to the geometrical requirements of the test methods [7].

The green samples were cold compressed and then heated up to 580 °C letting the particles move around, bond metallurgically and densify the aluminum based matrix. The sintering was carried out in a furnace heated at 5 °C/min and held for 2 h in a high purity argon atmosphere and then cooled under the same protective atmosphere. The controlled heat treatment was designed to promote bonding of the material, while avoiding oxidation, undesirable phase formation and excessive dimensional distortion. After sintering the specimens were checked for surface defects, cracks and changes in size. Their weights and sizes were recorded to observe how they shrank, remained the same size, and packed together before they were further characterized [7].

Sections were cut from pieces of each composition for metallographic characterization, mounted and ground with a sequence of silicon carbide abrasive papers of decreasing grade. After grinding, the surfaces were polished to a smooth finish suitable for optical microscopy, FESEM-EDS (field-emission scanning electron microscopy coupled with energy-dispersive X-ray spectroscopy) and microstructural examination. Scratches, surface deformation and ceramic particle pull-out were particularly important to minimize, as

*Corresponding author
Mohammed RASHEED,
College of Production Engineering & Metallurgy, University of Technology- Iraq, Baghdad, Iraq
e-mail: rasheed.mohammed40@yahoo.com

these could be confused with residual pores or inherent microstructural defects. To study the distribution of reinforcements, the morphology of the matrix, the interaction of surfaces and the variation of microstructures in some regions, many non-overlapping areas were examined [7].

Three specimens were prepared for each composition, resulting in a total of fifteen specimens for the five composite formulations (AMC0–AMC4). Several different microscopic fields were analyzed for each sample in an effort to determine the distribution in space of the ceramic reinforcements, the remaining porosity and the homogeneity of the microstructure. The experimental replicates were the samples prepared by different people, and the variation of microstructures in small areas of different specimens was observed by repeated microscopic observations. This method allowed us to look at differences between samples and give us a consistent way to compare how the ZrB_2–CeO_2 reinforcement content affected the way the material densed up and its microstructural features [7].

INSTRUMENTS AND EXPERIMENTAL CHARACTERIZATION EQUIPMENT

The experimental characterization of the Al–3Mg–1Zn/ZrB_2–CeO_2 hybrid composites was carried out using complementary microscopic, crystallographic, mechanical, and electrochemical techniques. Powder homogenization was performed using a FRITSCH Pulverisette 6 planetary ball mill (FRITSCH GmbH, Germany), while a uniaxial hydraulic press and a controlled-atmosphere furnace were employed for powder compaction and sintering, respectively. The processing parameters, including milling conditions, compaction pressure, sintering temperature, holding time, and atmosphere, are described in Sections 2.1 and 2.2 to avoid repetition.

Optical microstructural examination was performed using a ZEISS Axio Imager 2 optical microscope (Carl Zeiss Microscopy GmbH, Germany). Surface morphology and elemental composition were characterized using a Thermo Fisher Scientific Apreo 2 field-emission scanning electron microscope equipped with an energy-dispersive X-ray spectroscopy detector (FESEM–EDS; Thermo Fisher Scientific, USA). An accelerating voltage of 5–15 kV was employed according to the imaging and analytical requirements. Crystallographic orientation and grain-boundary characteristics were investigated using an SEM-integrated electron backscatter diffraction (EBSD) system, with orientation mapping conducted at step sizes of 0.1–0.2 μm. Phase identification and crystallographic characterization were performed using a Bruker D8 ADVANCE ECO X-ray diffractometer (Bruker AXS GmbH, Germany) equipped with Cu Kα radiation, operating over a 2θ range of 20–90° with a step size of 0.02°. Three-dimensional internal defects and pore distributions were examined using a ZEISS Xradia 620 Versa micro-computed tomography system (Carl Zeiss, Germany). Bulk density was determined using an analytical balance with Archimedes density-measurement accessories and a mass readability of 0.1 mg.

Mechanical characterization comprised Vickers hardness, nanoindentation, tensile testing, and compression testing. Vickers hardness measurements were performed using a calibrated hardness tester under an applied load of 4.903 N (HV0.5), with an indentation dwell time of 15 s. Nanoindentation measurements were conducted using an Anton Paar NHT^3 Nanoindentation Tester (Anton Paar, Austria), equipped with a diamond Berkovich indenter and operated at a maximum applied load of 5 mN. The indentation hardness and indentation modulus were determined from load-displacement curves using the Oliver-Pharr method. Tensile and compression tests were conducted using an Instron 5982 universal testing machine (Instron, USA) equipped with a calibrated load cell appropriate for the specimen geometry and expected loading range. Mechanical testing procedures were conducted under consistent experimental conditions to enable comparison of the five composite formulations.

Electrochemical measurements were performed using a Gamry Reference 600+ potentiostat/galvanostat (Gamry Instruments, USA) connected to a conventional three-electrode electrochemical cell. The composite specimens were used as working electrodes. Ag/AgCl electrode and platinum electrode were used as reference and counter electrodes, respectively. The tests were conducted in an aqueous NaCl solution at 3.5 wt.% . The open-circuit potential (OCP) was monitored for 3600 s, then potentiodynamic polarization measurements were performed at a potential scan rate of 0.5 mV/s. The obtained polarization curves were

*Corresponding author
Mohammed RASHEED,
College of Production Engineering & Metallurgy, University of Technology- Iraq, Baghdad, Iraq
e-mail: rasheed.mohammed40@yahoo.com

analyzed to determine the corrosion potential (E_{corr}) and the corrosion current density (i_{corr}). The same electrolyte conditions, working electrode surface preparation and exposed electrode area were used for the AMC0–AMC4 specimens to ensure comparability.

MICROSTRUCTURAL AND CRYSTALLOGRAPHIC EXAMINATION

In an effort to have a complete understanding of the microstructure and crystallographic characteristics of Al–3Mg–1Zn/ZrB_2–CeO_2 hybrid composites, optical microscopy (OM), field-emission scanning electron microscopy combined with energy-dispersive X-ray spectroscopy (FESEM–EDS), electron backscatter diffraction (EBSD) and X-ray diffraction (XRD) were applied. These two types of techniques were combined to investigate the shape of the grains, the distribution of the ceramic reinforcement, the clumping of the particles, the homogeneity of the elements, the crystallographic orientation and the phase constitution. We have studied the samples of each composition (AMC0–AMC4) under similar preparation and measurement conditions so that we can compare the changes in microstructure due to reinforcement [9].

Smooth cross sections were examined with an optical microscope using bright field illumination at three different magnifications. At least five separate fields were examined per specimen. The micrographs obtained were studied to evaluate the grain shape, the distribution of the reinforcements, the presence of any visible residual pores and the microstructural variations. High resolution morphological characterization was performed by FESEM with accelerating voltages in the range of 5–15 kV. By adjusting the working distance, detector configuration, magnification and image acquisition parameters of the SEM, good image quality and contrast were obtained. Energy-dispersive X-ray spectroscopy was used to investigate the spatial distribution of the elements Al, Mg, Zn, Zr, B, Ce and O. Element maps were generated from at least three representative areas of each separately made specimen. The electron micrographs along with elemental distributions were employed for the identification of ceramic-rich regions, matrix features and local compositional variation. The quantitative EDS results were considered independently from the chemical compositions used to prepare the powder [9].

The specimens were carefully polished and characterized according to crystallographic orientation, grain-size distributions, grain-boundary characteristics, and local lattice misorientation by electron backscatter diffraction. Orientation maps were constructed with a step size ranging from 0.1 to 0.2 μm, based on typical grain size and indexing quality. For grain size measurement, we used the equivalent-circle diameter method and identified high-angle grain boundaries with a misorientation threshold of ≥15°. Local orientation gradients and microstructural heterogeneity were investigated using kernel average misorientation (KAM) maps. To reduce measurement error as much as possible, the analysis examined the indexing fraction, pattern quality, and map-cleanup procedures. Statistical comparisons were performed at the level of independently fabricated specimens rather than treating individual EBSD pixels as independent experimental replicates [9].

X-ray diffraction analysis was performed using Cu Kα radiation over a 2θ range of 20–90°, with an angular step size of 0.02°. The stored diffraction patterns were analyzed to identify the crystalline phases corresponding to the Al–3Mg–1Zn matrix and the ZrB_2 –CeO_2 reinforcements. We also studied possible changes in phase composition after powder processing and sintering. The phase was determined by comparing the experimental diffraction peaks to the correct crystallographic reference data. The AMC0 composition was analyzed separately without reinforcement to distinguish the matrix-related diffraction features from the ceramic phases added to AMC1–AMC4. Peak-broadening analysis was used, with instrumental broadening and possible effects of crystallite size and lattice microstrain taken into account so that the diffraction-line widths were not taken too literally. The combined XRD and EBSD results provided complementary information on crystallographic structure and microstructural evolution across the composite series.

MECHANICAL TESTING

The mechanical properties of Al–3Mg–1Zn/ZrB_2–CeO_2 hybrid composites (AMC0–AMC4) were investigated by Vickers hardness testing, instrumented nanoindentation, uniaxial tensile testing and

*Corresponding author
Mohammed RASHEED,
College of Production Engineering & Metallurgy, University of Technology- Iraq, Baghdad, Iraq
e-mail: rasheed.mohammed40@yahoo.com

compression testing. Complementary methods were used to test the material's resistance to local indentation, its tensile strength, ductility and its ability to withstand compressive loads. Mechanical testing was performed on appropriately prepared specimens from each composition under consistent conditions to enable systematic comparison of the influence of ceramic reinforcement content on the mechanical performance of the composites [8].

Vickers Hardness was measured with an applied load of 4.903 N (HV0.5) and a dwell time of 15 s. Each specimen was prepared individually and had at least ten valid indentations, uniformly distributed on the polished area. The distance between the impressions and the edges of the specimen was sufficient to minimize interaction effects. The lengths of the diagonals of the residual impressions were measured and the hardness values were calculated using the standard Vickers hardness relation. The results were expressed as the mean hardness and standard deviation of the samples for each individual composition. The indentation of each sample was used to determine how the hardness changed in different regions [8].

The nanoindentation was measured with instruments equipped with a calibrated diamond Berkovich indenter with a maximum load of 5 mN. The area function of the indenter and the compliance of the instrument were calibrated prior to the test. Thermal drift and surface roughness were considered during the data collection and analysis. The load–displacement curves were recorded and analyzed by the Oliver–Pharr method for loading and unloading cycles to determine the indentation hardness (H), reduced elastic modulus (E), and contact stiffness (S). Each indentation was put away from the edges of the specimen, visible pores, and previous impressions to decrease errors of measurement. It was possible to obtain several indentations from different locations of each specimen in an effort to study the mechanical heterogeneity caused by the distribution of the ceramic reinforcement [8].

Specimens for the uniaxial tensile tests were prepared as per the requirements of ASTM E8/E8M. The dimensions, gage length, cross-sectional area, and strain measurement methods were all defined prior to the tests. The applied force and specimen elongation were recorded to produce engineering stress-strain curves. These curves were used to calculate the ultimate tensile strength (UTS), the yield strength (if calculable) and the elongation at fracture. For tests that may not be valid, fracture sites and specimen integrity were examined. To observe the effect of reinforcement content on tensile strength and ductility, the mechanical responses of samples prepared by different individuals were compared [8].

Cylindrical specimens of known initial diameters and heights were compressed at a constant loading rate and proper platen alignment. The engineering compressive stress and strain were computed from the applied load, the initial cross-sectional area and the deformation of the specimen. The obtained stress-strain curves were studied to determine the compressive strength of the material and its deformation. The energy density for the compressive energy absorption was calculated by combining the experimentally recorded stress–strain responses up to a common strain limit. The specimen was kept at a constant height-to-diameter ratio and loading conditions to minimize geometrical and frictional effects. Mechanical results were summarized using specimen-level mean values and standard deviations to distinguish independent experimental variability from repeated measurements within individual specimens [8].

OPEN-CIRCUIT POTENTIAL STABILIZATION AND POTENTIODYNAMIC POLARIZATION

The electrochemical corrosion behavior of the Al–3Mg–1Zn/ZrB_2–CeO_2 hybrid composites (AMC0–AMC4) was investigated using open-circuit potential (OCP) monitoring and potentiodynamic polarization measurements in an aqueous 3.5 wt.% NaCl solution at 25 ± 1 °C. Measurements were made with a Gamry Reference 600+ potentiostat/galvanostat connected to a standard three-electrode electrochemical cell. The prepared composite specimens served as the working electrodes (WE), while an Ag/AgCl electrode and a platinum-mesh electrode were employed as the reference electrode (RE) and counter electrode (CE), respectively. The working electrodes were positioned such that only a small part of the electrolyte was in contact with them (approximately 1 cm^2). The rest of the surfaces of the samples were electrically insulated to prevent unwanted electrochemical reactions [11].

*Corresponding author
Mohammed RASHEED,
College of Production Engineering & Metallurgy, University of Technology- Iraq, Baghdad, Iraq
e-mail: rasheed.mohammed40@yahoo.com

Prior to the electrochemical tests, the surfaces of the exposed specimens were ground and polished several times to a uniform finish. The electrodes were cleaned, washed and dried and then immersed in the electrolyte. The open-circuit potential was continuously monitored for 3600 s to observe the evolution of the electrode potential and its stability under free corrosion of the metal. The OCP-time curves were prepared to study the electrochemical stability and the changes of the composite surfaces in the presence of chloride. The OCP values were presented against the Ag/AgCl reference electrode and were not the same as the corrosion potentials which were determined later by measuring potentiodynamic polarization [11].

Potentiodynamic polarization measurements were performed at a potential scan rate of 0.5 mV/s after OCP monitoring. Polarization curves were recorded in the experimentally selected potential range in relation to the stable OCP. The curves covered the right cathodic and anodic regions to study the electrochemical behavior. The acquired current data were normalized to the exposed electrode area to obtain current density, and the polarization curves were analyzed to determine the corrosion potential (E_{corr}) and corrosion current density (i_{corr}). Where clearly defined Tafel regions were available, the corresponding anodic and cathodic branches were evaluated by Tafel extrapolation. The electrochemical response of the five compositions was compared in terms of potential evolution, polarization characteristics, and corrosion-current behavior to examine the influence of ZrB_2–CeO_2 reinforcement content on corrosion resistance [11].

The experimental three-electrode configuration used for OCP monitoring and potentiodynamic polarization measurements is schematically presented in Fig. 2. The arrangement consists of the Al–3Mg–1Zn/ZrB_2–CeO_2 composite working electrode, Ag/AgCl reference electrode, and platinum-mesh counter electrode connected to the potentiostat/galvanostat. All electrochemical measurements were conducted under consistent electrolyte composition, exposed electrode area, temperature, and surface-preparation conditions to ensure direct comparability among the five composite formulations [11]

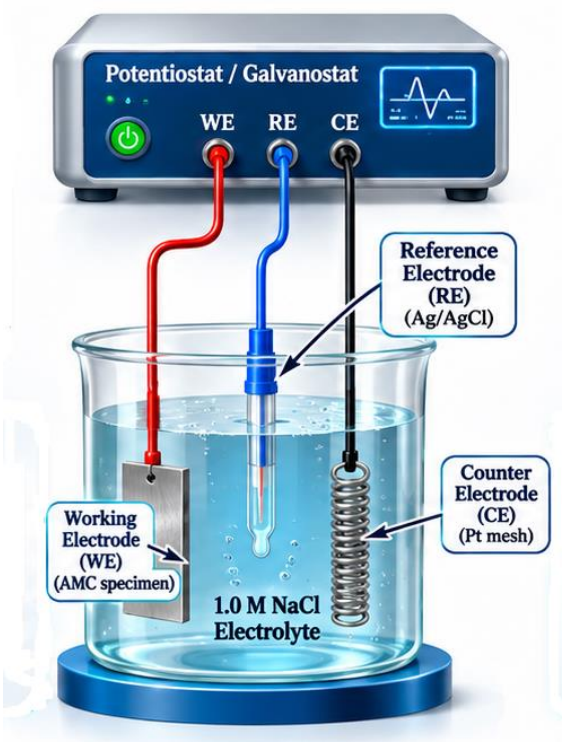


Fig. 2. Schematic representation of the three-electrode electrochemical cell employed for open-circuit potential (OCP) monitoring and potentiodynamic polarization measurements of Al–3Mg–1Zn/ZrB_2–CeO_2 hybrid composites.

*Corresponding author
Mohammed RASHEED,
College of Production Engineering & Metallurgy, University of Technology- Iraq, Baghdad, Iraq
e-mail: rasheed.mohammed40@yahoo.com

RESULTS AND DISCUSSION

POWDER-SIZE AND OPTICAL MICROSTRUCTURE EVOLUTION

The particle-size distribution and optical microstructural characteristics of the Al–3Mg–1Zn/ZrB_2–CeO_2 hybrid composites were systematically investigated to evaluate the influence of ceramic reinforcement content on powder morphology, particle agglomeration, and microstructural evolution. The five compositions (AMC0–AMC4) were compared to establish relationships between reinforcement concentration, powder-size characteristics, matrix continuity, and the distribution of microstructural features following powder processing and sintering. Particular attention was directed toward identifying changes in particle clustering and microstructural homogeneity associated with increasing ZrB_2–CeO_2 content [12].

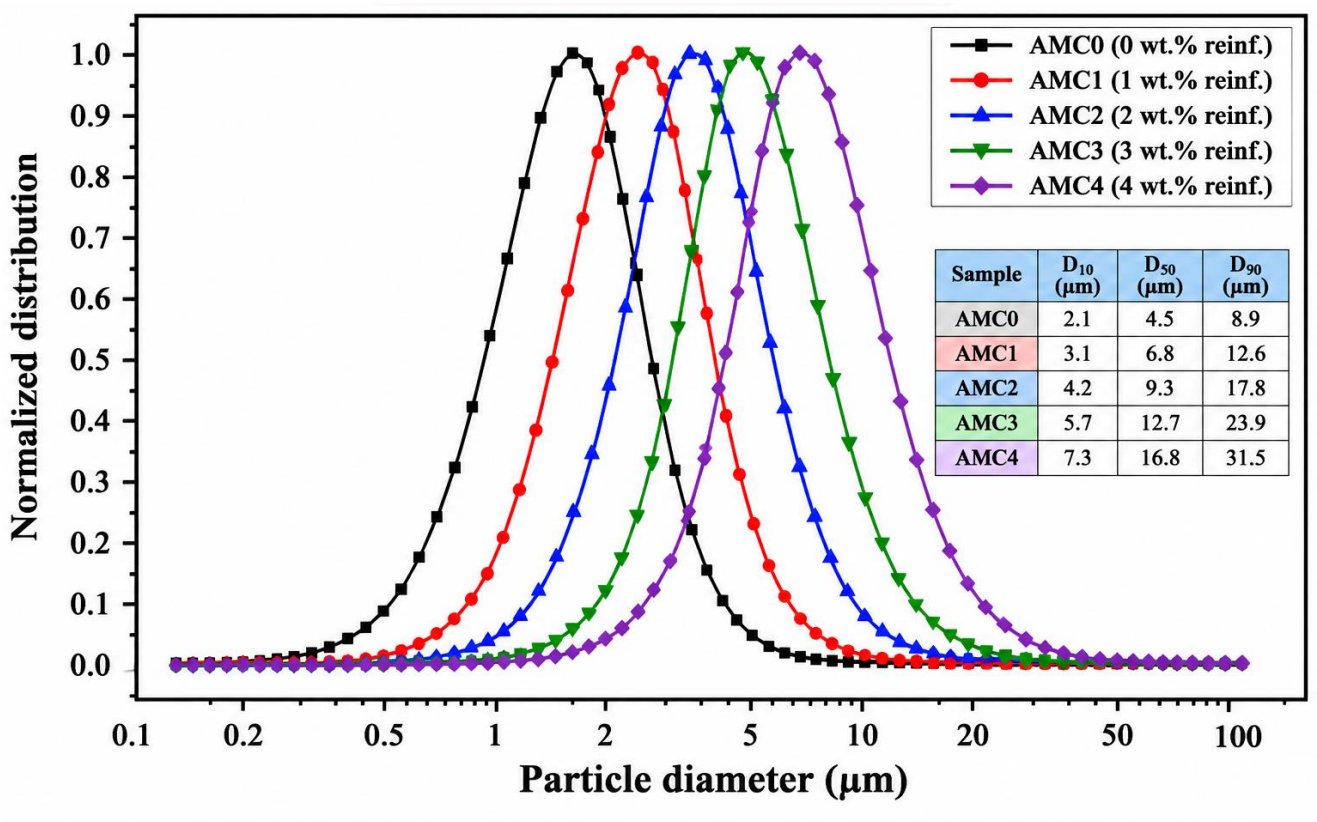
Fig. 3. Particle size distribution curves of the five composite powder mixtures. The median particle diameter (D50) of AMC0 was 4.5 μm and that of AMC4 was 16.8 μm, an increase of about 3.73 times. D10 values ranged from 2.1 to 7.3 μm and D90 values ranged from 8.9 to 31.5 μm (Table 2). As the content of the ceramic reinforcement increases, it is reasonable that the particles become larger due to their clustering and sticking together more during powder homogenization. The observed behavior could be attributed to the combined effect of particle breakage, cold welding and the interactions of ceramic particles with the metal matrix during mechanical milling. The wider particle size distribution observed at higher reinforcement concentration may influence the packing of the powder, the interaction between the particles and the density of the material during sintering [13].

The optical micrographs in Fig. 4 illustrate the changes in microstructural morphology and reinforcement distribution with composition. The non-reinforced AMC0 specimen had a fairly uniform metallic matrix, but the reinforced specimens had increasing concentrations of second-phase features. AMC1 and AMC2 had scattered reinforcement rich areas. However, AMC3 had a better balance between the particle distribution and matrix continuity. AMC4 showed more pronounced particle clustering and microstructural heterogeneity, indicating that excessive ceramic addition may reduce the uniformity of dispersion and create regions of unconsolidated concrete. The results indicate that the amount of reinforcements used has a great influence on the microstructural properties of the sintered composites obtained [13].

The differences in the microstructures of the five compositions were studied using quantitative image analysis. Figure 5 (a–e) Equivalent-diameter distributions of segmented microstructural features for AMC0–AMC4. (f) Corresponding dark feature area fractions. The summary of the numerical parameters is presented in Table 3. The segmented-feature distributions indicated changes in the size and location of the features with the increase in the reinforcement content. The dark feature area fractions gave us more information on the location of the low intensity areas. To interpret the dark feature area fractions as porosity we need to be able to distinguish between real pores, ceramic particles, surface relief and pull-out due to polishing. Therefore, the image analysis results were considered together with the optical observations and the results of the complementary microstructural characterization [14].

The results of particle-size distribution and optical microstructure indicate that the ceramic reinforcement content changes the clumping of the powder, the uniformity of the microstructure and cohesiveness of the matrix in the Al–3Mg–1Zn/ZrB_2–CeO_2 composites. Based on the trends observed, an intermediate reinforcement concentration may be optimal for balancing ceramic dispersion and microstructural uniformity. Higher ceramic loading, however, could result in clustering and local heterogeneity. These results give insight into the variations in density and mechanical properties discussed in the following sections [14].

*Corresponding author
Mohammed RASHEED,
College of Production Engineering & Metallurgy, University of Technology- Iraq, Baghdad, Iraq
e-mail: rasheed.mohammed40@yahoo.com



Sample	D_{10} (μm)	D_{50} (μm)	D_{90} (μm)
AMC0	2.1	4.5	8.9
AMC1	3.1	6.8	12.6
AMC2	4.2	9.3	17.8
AMC3	5.7	12.7	23.9
AMC4	7.3	16.8	31.5

Fig. 3. Experimentally determined particle-size distributions of Al–3Mg–1Zn/ZrB_2–CeO_2 composite powder mixtures (AMC0–AMC4), including D10, D50, and D90 particle-size parameters.

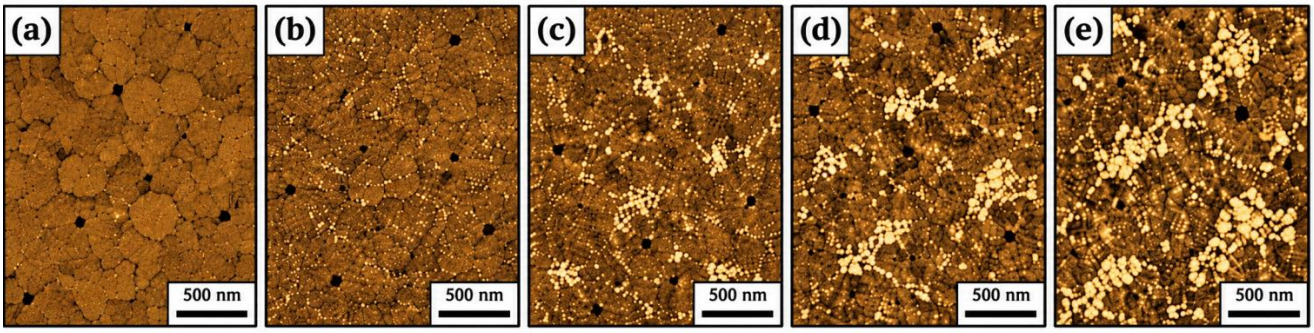


Fig. 4. Optical micrographs showing microstructural evolution of Al–3Mg–1Zn/ZrB_2–CeO_2 hybrid composites with increasing ceramic reinforcement content: (a) AMC0, (b) AMC1, (c) AMC2, (d) AMC3, and (e) AMC4.

*Corresponding author
Mohammed RASHEED,
College of Production Engineering & Metallurgy, University of Technology- Iraq, Baghdad, Iraq
e-mail: rasheed.mohammed40@yahoo.com

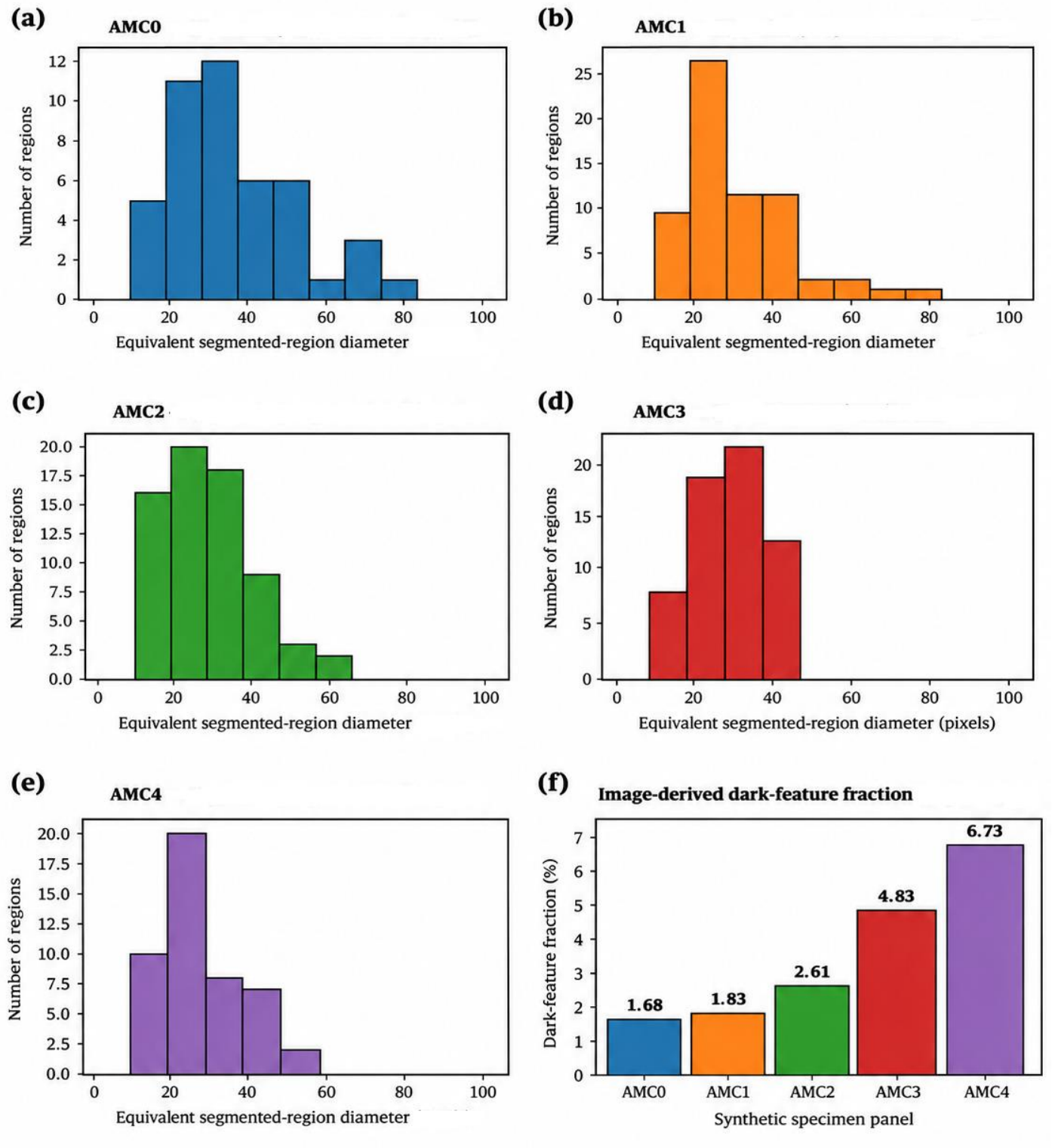


Fig. 5. Quantitative image analysis of the AMC0–AMC4 composite microstructures: (a–e) equivalent-diameter distributions of segmented features and (f) corresponding dark-feature area fractions.

Tables 2 and 3 summarize the particle-size distribution parameters and quantitative microstructural characteristics, respectively, of the five Al–3Mg–1Zn/ZrB_2–CeO_2 composite formulations (AMC0–AMC4), enabling a systematic comparison of reinforcement-dependent variations in powder morphology and microstructural features.

*Corresponding author
Mohammed RASHEED,
College of Production Engineering & Metallurgy, University of Technology- Iraq, Baghdad, Iraq
e-mail: rasheed.mohammed40@yahoo.com

Table 2. Experimentally determined particle-size distribution parameters (D10, D50, and D90) of AMC0–AMC4 powder mixtures.

Sample	Ceramic (wt.%)	D10 (μm)	D50 (μm)	D90 (μm)
AMC0	0	2.1	4.5	8.9
AMC1	1	3.1	6.8	12.6
AMC2	2	4.2	9.3	17.8
AMC3	3	5.7	12.7	23.9
AMC4	4	7.3	16.8	31.5

Table 3. Quantitative image-analysis parameters and dark-feature area fractions of AMC0–AMC4 hybrid composites.

Sample	Dark-feature area (%)	Segmented regions (n)	Median diameter (pixels)
AMC0	1.68	45	37.96
AMC1	1.83	67	29.10
AMC2	2.61	68	27.99
AMC3	4.83	62	31.14
AMC4	6.73	47	27.22

FESEM–EDS DISTRIBUTION OF THE HYBRID REINFORCEMENT

The surface morphology and elemental distribution of the Al–3Mg–1Zn/ZrB_2–CeO_2 hybrid composites were systematically investigated using field-emission scanning electron microscopy coupled with energy-dispersive X-ray spectroscopy (FESEM–EDS). The micrographs presented in Fig. 6(a–e) reveal composition-dependent variations in matrix morphology, particulate distribution, and microstructural heterogeneity across AMC0–AMC4. The AMC0 unreinforced specimen has a mostly continuous metallic matrix while the reinforced specimens have second-phase features that become more concentrated with time. AMC1 and AMC2 have particulate regions, however AMC3 has a more uniform distribution of reinforcement rich features. In contrast, AMC4 shows higher particle clustering and localized morphology heterogeneity which suggests that increasing ceramic content can vary the dispersion of reinforcements and the matrix cohesion [15].

A more detailed comparison of the FESEM morphological features, and the corresponding segmented-feature size distributions is presented in Fig. 7(a–e). Changes in the shape and position of features suggest that the five composite formulations exhibit different levels of local particle clustering. The features of lower reinforcement concentrations are more spread out, whereas the features of higher ceramic contents are more concentrated in clustered areas. The changes in shapes can be explained by the variation in packing of the particles, the interaction of the particles with each other and the balance between the reinforcement dispersion and agglomeration during the powder processing. The segmented-feature distributions provide a quantitative description of the local microstructural heterogeneity [16] if the image dimensions are calibrated and the same segmentation criteria are used.

Quantitative image analysis indicates that the dark-feature area fraction increases from 1.68% for AMC0 to 1.83%, 2.61%, 4.83%, and 6.73% for AMC1, AMC2, AMC3, and AMC4, respectively. The difference between AMC4 and AMC0 is 5.05 percentage points, equal to an increase of 4.01 times. This gradual change as the reinforcement content increases suggests that there are more low intensity areas in the micrographs examined. In such areas, pores, particle-associated surface relief, or other features may provide contrast. The dark-feature area fraction is therefore considered a morphological parameter extracted from the image and not a direct measure of porosity unless the segmented features have been verified by a third

*Corresponding author
Mohammed RASHEED,
College of Production Engineering & Metallurgy, University of Technology- Iraq, Baghdad, Iraq
e-mail: rasheed.mohammed40@yahoo.com

party. The accompanying measurements of densification and internal defects allow us to assess the effect of ceramic loading on the amount of residual porosity [17].

Table 4 presents the quantitative morphological parameters and reveals that the quantity of reinforcement affects the distribution of the particulate features. The percentage of bright features increases from 3.21% for AMC0 to 23.76% for AMC4; the average distance between particles decreases from 312.4 nm to 98.3 nm. The characteristic cluster-size parameter also increases from 63.7 nm to 214.8 nm with the progress of the composition series. These trends indicate that at higher reinforcement contents particle rich regions are coming nearer to each other and there is less space between identified features. Such changes are consistent with the notion that as the ceramic loading increases, the particles will interact and adhere to each other more. However, to confirm that particular bright features are due to ZrB_2 or CeO_2, they must be correlated with other elements and phases [16].

The EDS spectra and elemental-distribution maps (Figs. 8–11) give further details on the chemical composition of the reinforced composites. Elemental analysis was carried out to find the presence of Al, Mg and Zn in the metal matrix and to study the distribution of Zr, B, Ce and O in the ceramic reinforcements. The morphological features in the electron micrographs of Zr-rich and Ce-rich regions were compared with each other in space to see how much reinforcement was spread out. Boron signals should be interpreted with extra caution, because its detection and quantification may be affected by the capabilities of the detector, absorptivity and the specimen conditions. Accordingly, the EDS findings were considered together with XRD phase identification to distinguish reinforcement-associated elements from confirmed crystalline phases [17].

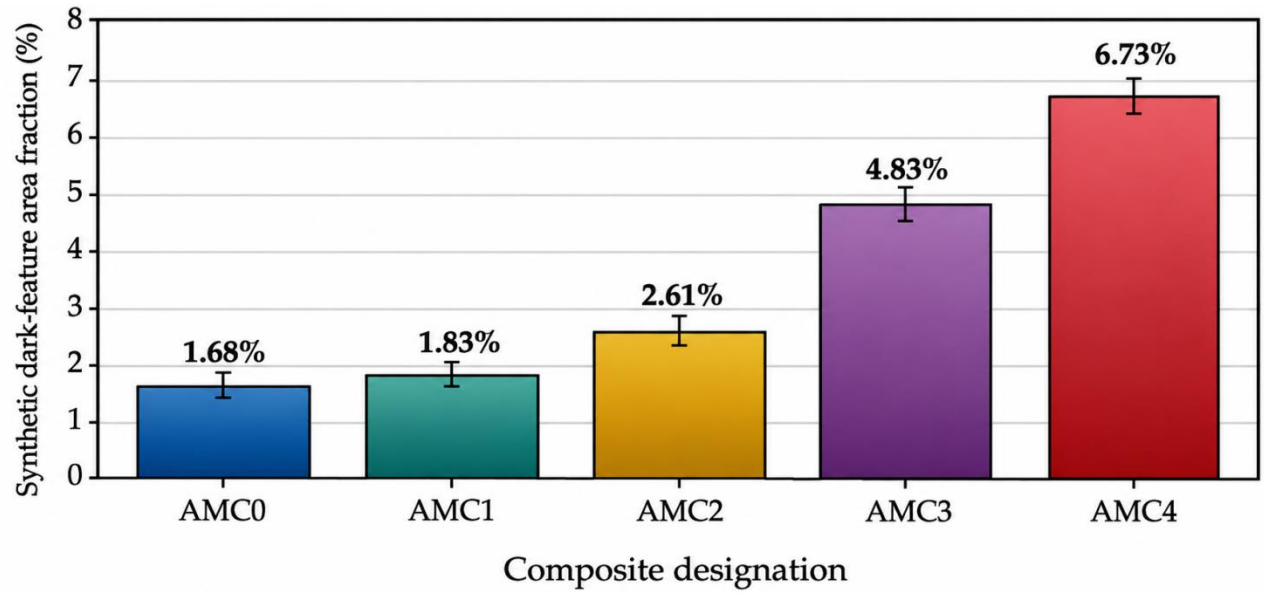


Fig. 6. FESEM micrographs illustrating the surface morphology and reinforcement distribution of Al–3Mg–1Zn/ZrB_2–CeO_2 hybrid composites: (a) AMC0, (b) AMC1, (c) AMC2, (d) AMC3, and (e) AMC4.

*Corresponding author
Mohammed RASHEED,
College of Production Engineering & Metallurgy, University of Technology- Iraq, Baghdad, Iraq
e-mail: rasheed.mohammed40@yahoo.com

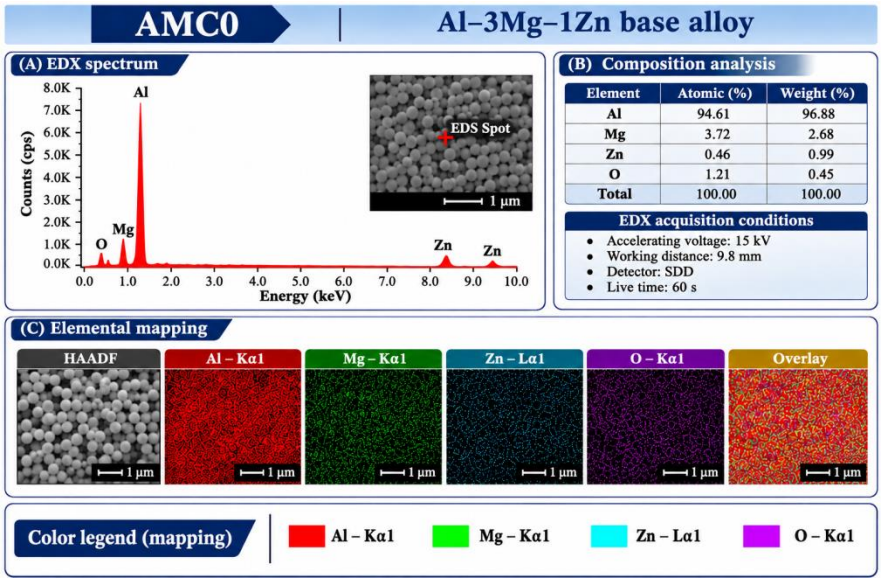


Fig. 7. FESEM morphological characterization and quantitative segmented-feature size distributions of the five Al–3Mg–1Zn/ZrB_2–CeO_2 composite formulations AMC0.

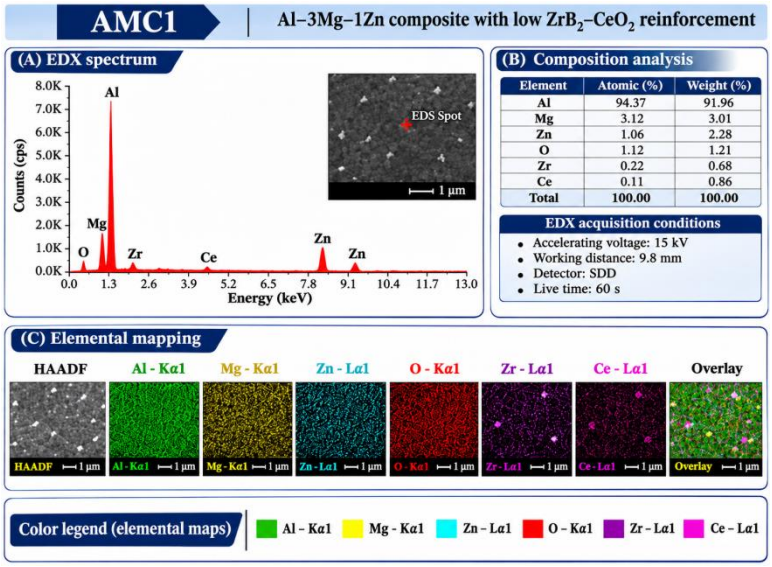


Fig. 8. FESEM morphological characterization and quantitative segmented-feature size distributions of the five Al–3Mg–1Zn/ZrB_2–CeO_2 composite formulations AMC1.

*Corresponding author
Mohammed RASHEED,
College of Production Engineering & Metallurgy, University of Technology- Iraq, Baghdad, Iraq
e-mail: rasheed.mohammed40@yahoo.com

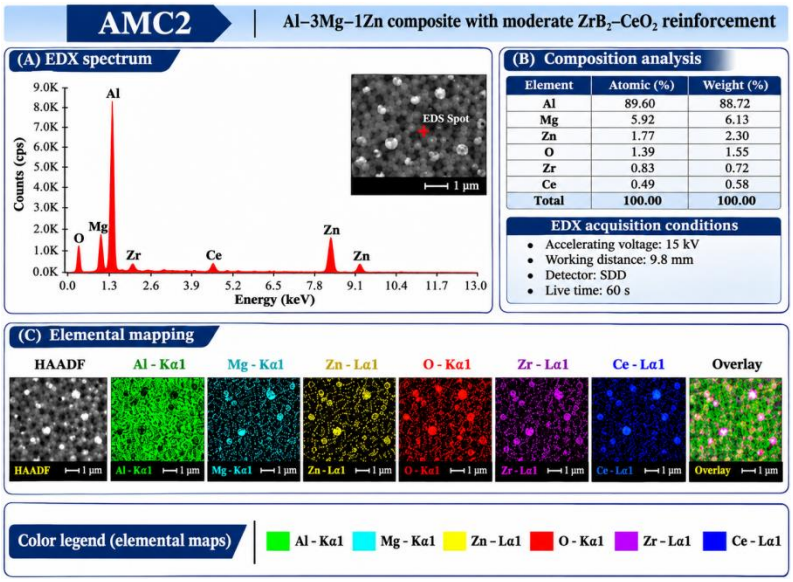


Fig. 9 FESEM morphological characterization and quantitative segmented-feature size distributions of the five Al–3Mg–1Zn/ZrB_2–CeO_2 composite formulations AMC2.

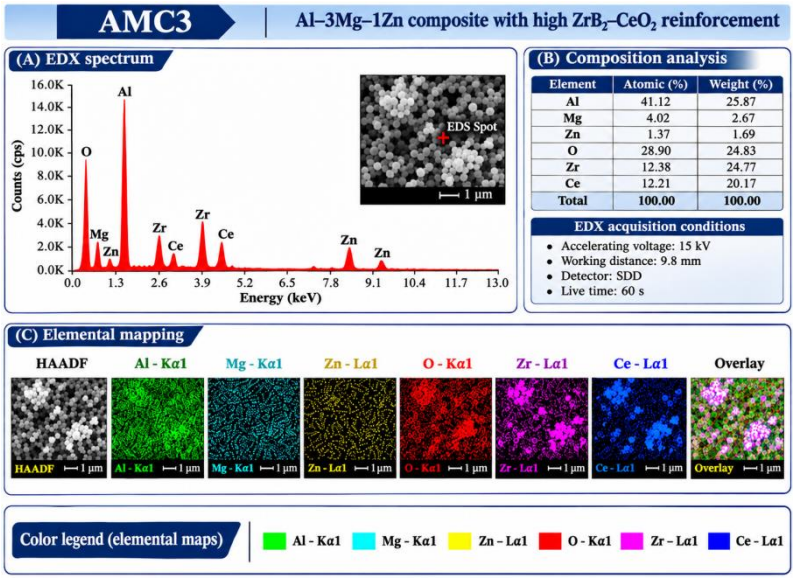


Fig. 10. FESEM morphological characterization and quantitative segmented-feature size distributions of the five Al–3Mg–1Zn/ZrB_2–CeO_2 composite formulations AMC3.

*Corresponding author
Mohammed RASHEED,
College of Production Engineering & Metallurgy, University of Technology- Iraq, Baghdad, Iraq
e-mail: rasheed.mohammed40@yahoo.com

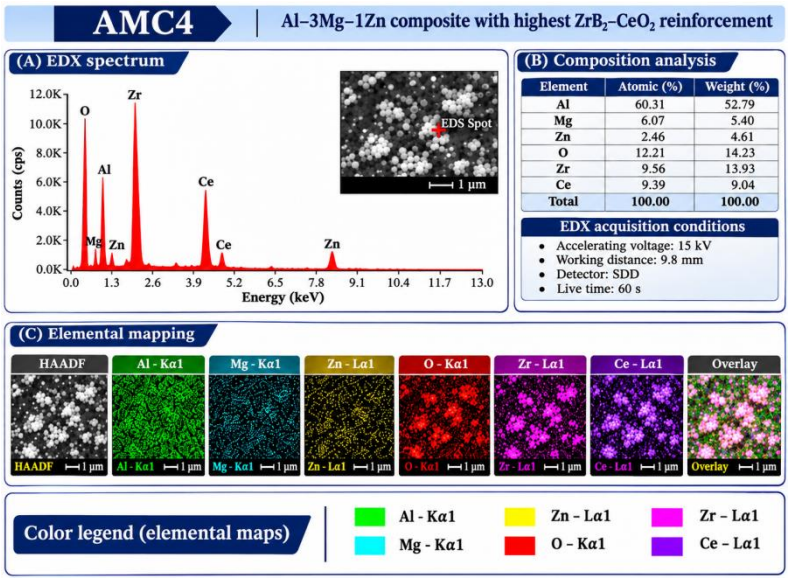


Fig. 11. FESEM morphological characterization and quantitative segmented-feature size distributions of the five Al–3Mg–1Zn/ZrB_2–CeO_2 composite formulations AMC4.

Table 4. Quantitative FESEM image-analysis parameters of Al–3Mg–1Zn/ZrB_2–CeO_2 hybrid composites (AMC0–AMC4), including bright-feature area fraction, interparticle spacing, and characteristic cluster size.

Image-derived descriptor	AMC0	AMC1	AMC2	AMC3	AMC4
Dark-feature fraction (%)	1.68	1.83	2.61	4.83	6.73
Bright particle area fraction (%)	3.21	6.04	10.27	15.93	23.76
Pore-like size D10/D50/D90 (nm)	25/41/72	27/45/78	31/56/101	39/72/129	46/89/163
Circularity, C	0.86 ± 0.09	0.84 ± 0.08	0.82 ± 0.08	0.80 ± 0.09	0.77 ± 0.10
Aspect ratio, AR	1.18 ± 0.21	1.21 ± 0.23	1.26 ± 0.27	1.31 ± 0.30	1.37 ± 0.35
Interparticle spacing (nm)	312.4 ± 76.1	237.8 ± 61.3	178.6 ± 48.5	135.9 ± 41.2	98.3 ± 35.7
Cluster size (nm)	63.7 ± 24.5	82.5 ± 29.8	107.4 ± 37.6	153.9 ± 55.2	214.8 ± 78.9
Line-feature density (μm^{-1})	0.004	0.006	0.011	0.018	0.028
Homogeneity index, H	0.965	0.957	0.941	0.916	0.887

EBSD GRAIN SIZE AND LOCAL ORIENTATION

Electron backscatter diffraction (EBSD) characterization was performed to investigate the crystallographic orientation, grain-size distribution, grain-boundary characteristics, and local orientation gradients of the Al–3Mg–1Zn/ZrB_2–CeO_2 hybrid composites (AMC0–AMC4). The compositions investigated are shown by the inverse pole figure (IPF-Z) orientation maps, kernel average misorientation (KAM) distributions and grain-size histograms in Figure 12(a–e). The orientation maps show the changes in the reconstructed aluminum-matrix grain structure with increasing ceramic reinforcement content [18].

The quantitative EBSD results summarized in Table 5 indicate average grain diameters of 2.8, 2.5, 2.2, 2.9, and 3.4 µm for AMC0, AMC1, AMC2, AMC3, and AMC4, respectively. From AMC0 to AMC2, the grain diameter is becoming smaller and smaller until it reaches the minimum of 2.2 µm in AMC2. This is a decrease of about 21.4% compared with the non-reinforced composition. The average grain diameters increase with increase in ceramic content. For AMC3 the increase is 2.9 µm and for AMC4 it is 3.4 µm. The increase is approximately 3.6% for AMC3 and 21.4% for AMC4. The nonmonotonic trend shows that a small amount of ceramic may be beneficial to limit the growth of matrix grains, while higher reinforcement concentrations may reduce the effectiveness of grain boundary restriction by changing the distribution of particles, their clustering and local adhesion [19].

*Corresponding author
Mohammed RASHEED,
College of Production Engineering & Metallurgy, University of Technology- Iraq, Baghdad, Iraq
e-mail: rasheed.mohammed40@yahoo.com

Fig. 12 KAM maps give additional information on differences in crystallographic orientation in the aluminum matrix. Table 5 shows that the average KAM values for AMC0, AMC1, AMC2, AMC3 and AMC4 are 1.42°, 1.26°, 1.11°, 1.58° and 1.83° respectively. AMC2 has the lowest mean KAM value of 1.11°, a decrease of about 21.8% compared to AMC0 . The average KAM values of AMC3 and AMC4 are higher, 1.58° and 1.83° respectively. AMC4 is higher by about 28.9% than AMC0. These changes show the differences in spatial spreading of local orientation gradients and intragranular crystallographic heterogeneity . The increased KAM values at higher reinforcement concentrations could be associated with different types of local deformation, interfacial constraints, or residual strain gradients [20].

The EBSD results, together with the mechanical-property changes, point to an important difference. The AMC3 exhibits lowest values for mean KAM and average grain diameter, but highest values for hardness and tensile strength in the mechanical-property dataset. The mean grain diameter and mean KAM of AMC3 are 2.9 μm and 1.58°, respectively, which are larger than those of AMC0 (2.8 μm and 1.42°). These results indicate that the improved mechanical properties of AMC3 cannot be attributed solely to grain refinement. Other contributions, including improved densification, effective load transfer between the ceramic reinforcements and metallic matrix, differences in reinforcement spacing, and local resistance to plastic deformation, may also influence the overall response [20].

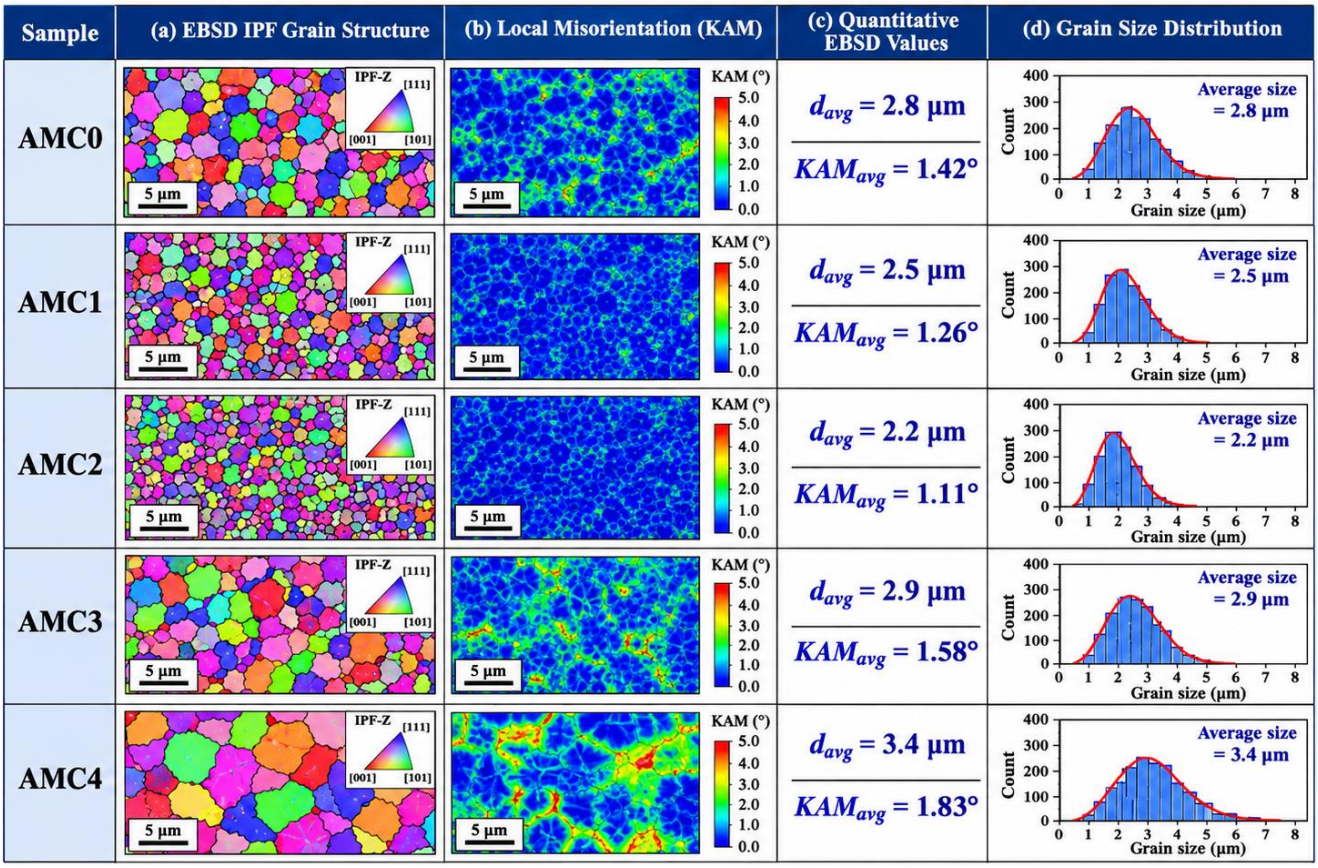


Fig. 12. EBSD characterization of Al–3Mg–1Zn/ZrB_2–CeO_2 hybrid composites: (a) AMC0, (b) AMC1, (c) AMC2, (d) AMC3, and (e) AMC4, showing inverse pole figure (IPF-Z) orientation maps, kernel average misorientation (KAM) distributions, and reconstructed grain-size histograms.

Table 5 summarizes the experimentally determined average grain diameters and mean kernel average misorientation (KAM) values of the five Al–3Mg–1Zn/ZrB_2–CeO_2 hybrid composites (AMC0–AMC4), highlighting the influence of ceramic reinforcement content on grain structure and local crystallographic misorientation.

*Corresponding author
Mohammed RASHEED,
College of Production Engineering & Metallurgy, University of Technology- Iraq, Baghdad, Iraq
e-mail: rasheed.mohammed40@yahoo.com

Table 5. Average grain diameter and mean kernel average misorientation (KAM) of Al–3Mg–1Zn/ZrB_2–CeO_2 hybrid composites (AMC0–AMC4)

Sample	Mean grain diameter (μm)	Mean KAM (°)	Grain size vs AMC0 (%)	KAM vs AMC0 (%)
AMC0	2.8	1.42	Reference	Reference
AMC1	2.5	1.26	-10.7	-11.3
AMC2	2.2	1.11	-21.4	-21.8
AMC3	2.9	1.58	+3.6	+11.3
AMC4	3.4	1.83	+21.4	+28.9

XRD PHASE IDENTIFICATION AND CRYSTALLITE-SIZE ANALYSIS

X-ray diffraction (XRD) analysis was performed to investigate the crystalline phase composition, structural evolution, and coherent diffraction-domain size of the Al–3Mg–1Zn/ZrB_2–CeO_2 hybrid composites (AMC0–AMC4). The diffraction patterns presented in Fig. 13 exhibit the characteristic reflections of face-centered cubic α-Al at approximately 2θ = 38.4°, 44.7°, 65.1°, and 78.2°, corresponding to the (111), (200), (220), and (311) crystallographic planes, respectively. It was found that these reflections are the main diffraction features of the high aluminum metal matrix throughout the entire composition series. The reinforced specimens showed extra diffraction patterns related to the added ceramic parts, which suggested that the phase composition changed with the increase of the ZrB_2–CeO_2 content [21].

The diffraction patterns of AMC1–AMC4 present a reflection at about 2θ = 28.6° corresponding to the (111) plane of cubic CeO_2 and a feature at about 34.6° which is attributed to ZrB_2. The intensity of the diffraction patterns related to the reinforcement varied with the loaded ceramic, since these phases contributed differently to the overall diffraction response . No reflections related to the intentionally added ceramic phases were observed for the non-reinforced AMC0 sample. Another weak feature was observed around 42.7° and it was attributed to an intermetallic phase comprising Mg and Zn. Conversely, the identification of $MgZn_2$ and ZrB_2 requires agreement with additional characteristic reflections and proper crystallographic reference patterns, since different diffraction peaks may overlap [21].

From the diffraction profiles, it was observed that the five compositions showed different peak widths and intensity levels. AMC1 and AMC2 showed relatively narrow matrix-related reflections, whereas AMC3 and AMC4 showed wider diffraction features. These variations can be attributed to changes in the coherent diffraction domain size, lattice microstrain, distortions caused by defects, or contributions from multiple phases. Diffraction-peak broadening can be caused by a number of things and so the relative peak widths were interpreted in terms of the corresponding line-profile calculations rather than being attributed only to structural disorder or grain refinement [22].

The size of the apparent crystallite was estimated by the Scherrer relationship as shown in Equation (1). The calculation included the X-ray wavelength, diffraction angle and full width at half maximum (FWHM), with allowance for instrumental broadening. The wavelength of the Cu K+-radiation was fixed at ~0.15406 nm and the shape factor was chosen according to the peak-profile model used. This yields the average coherent diffraction-domain sizes, which are different from the physical sizes of whole metallic grains [22]

$$2d\ sin\theta\ =\ n\lambda \quad (1)$$

where (d) is the interplanar spacing between adjacent crystallographic planes (nm), (θ) is the Bragg diffraction angle corresponding to half of the measured (2θ) value, (n) is the diffraction order (typically (n=1), and (λ) is the wavelength of the incident X-ray radiation (0.15406 nm for Cu Kα radiation). The calculated interplanar spacings were used to support the identification of crystalline phases by comparison with standard crystallographic reference data.

*Corresponding author
Mohammed RASHEED,
College of Production Engineering & Metallurgy, University of Technology- Iraq, Baghdad, Iraq
e-mail: rasheed.mohammed40@yahoo.com

The approach provides complementary structural information to the Scherrer calculation, although its quantitative interpretation depends on the validity of the adopted peak-shape and isotropic-strain assumptions [22].

$$D = \frac{K\lambda}{\beta \cos\theta} \quad (2)$$

The shape factor is typically ~ 0.9. X-ray wavelength is 0.15406 nm for Cu K± radiation. The full width at half maximum (FWHM) of the selected diffraction peak after correcting for instrument broadening is given in radians. The Bragg angle is given. If you believe that the broadening is mostly due to the finite dimensions of the domains, the Scherrer relation can give you an idea of the size of a coherent diffraction domain. Thus, the influence of lattice microstrain and other broadening sources should be considered in the interpretation of the calculated values.

The crystallographic parameters reported in Table 6 allow a comparison of the five composite formulations on a quantitative basis. The AMC0 reference composition exhibited an average coherent diffraction-domain size of 38.40 nm, based on the selected aluminum-matrix reflections. The variations in the corresponding crystallite-size parameters across AMC1–AMC4 were evaluated alongside the diffraction-line widths and identified phase contributions.

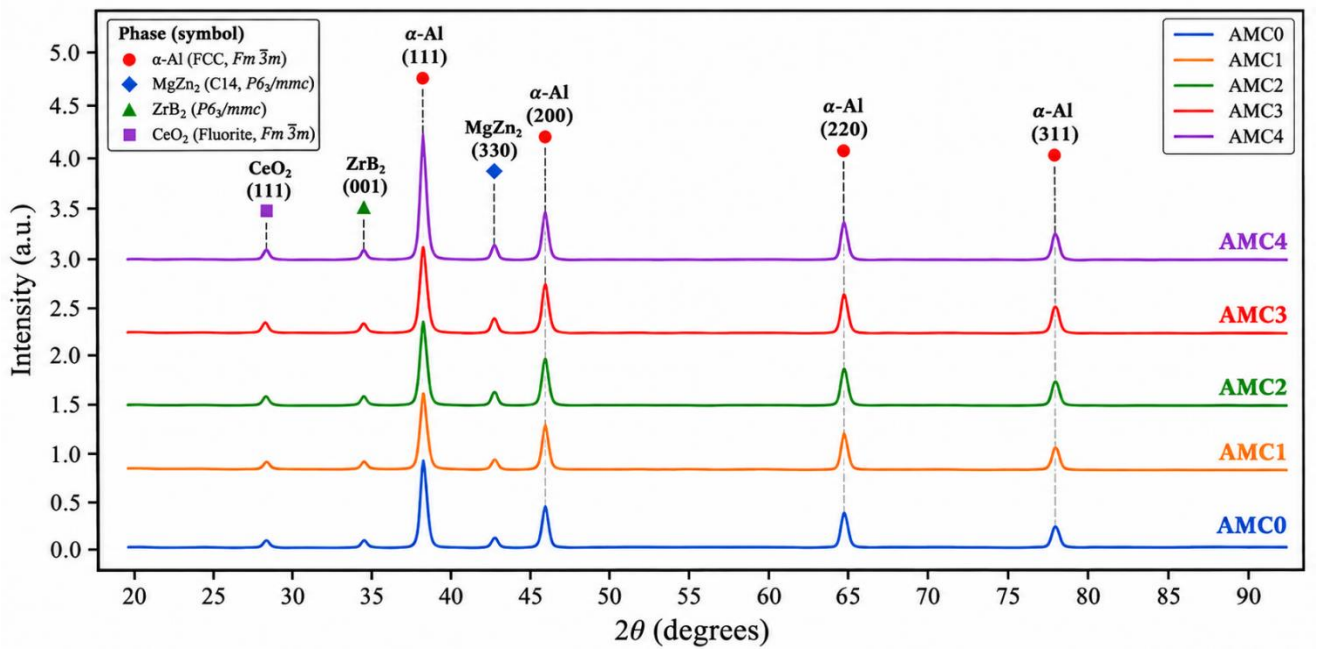


Fig. 13. X-ray diffraction patterns of Al–3Mg–1Zn/ZrB_2–CeO_2 hybrid composites (AMC0–AMC4), showing the principal α-Al reflections and reinforcement-associated diffraction features.

Table 6 summarizes the crystalline phase assignments and XRD-derived crystallite-size parameters of the five Al–3Mg–1Zn/ZrB_2–CeO_2 hybrid composites (AMC0–AMC4), providing a quantitative comparison of reinforcement-dependent variations in phase constitution and coherent diffraction-domain size.

*Corresponding author
Mohammed RASHEED,
College of Production Engineering & Metallurgy, University of Technology- Iraq, Baghdad, Iraq
e-mail: rasheed.mohammed40@yahoo.com

Table 6. Crystalline phase assignments and XRD-derived coherent diffraction-domain sizes of Al–3Mg–1Zn/ZrB_2–CeO_2 hybrid composites (AMC0–AMC4).

Samples	2θ (°)	FWHM	(hkl)	d-Spacing (Å)	Dcs (nm)	Dcs-ave (nm)
AMC0	38.47	0.23	(111)	2.3382	36.58	38.40
AMC0	44.74	0.24	(200)	2.0240	35.79	
AMC0	65.10	0.22	(220)	1.4317	42.84	
AMC1	28.56	0.29	(111)	3.1229	28.27	35.91
AMC1	34.56	0.27	(001)	2.5932	30.81	
AMC1	38.45	0.22	(111)	2.3394	38.24	
AMC1	44.72	0.23	(200)	2.0248	37.35	
AMC1	65.08	0.21	(220)	1.4321	44.87	
AMC2	28.57	0.27	(111)	3.1218	30.36	38.74
AMC2	34.58	0.25	(001)	2.5918	33.28	
AMC2	38.43	0.20	(111)	2.3405	42.06	
AMC2	44.70	0.21	(200)	2.0257	40.90	
AMC2	65.06	0.20	(220)	1.4325	47.11	
AMC3	28.59	0.31	(111)	3.1197	26.45	33.10
AMC3	34.60	0.29	(001)	2.5903	28.69	
AMC3	38.41	0.24	(111)	2.3417	35.05	
AMC3	44.68	0.25	(200)	2.0266	34.36	
AMC3	65.04	0.23	(220)	1.4329	40.96	
AMC4	28.61	0.34	(111)	3.1176	24.11	29.63
AMC4	34.63	0.32	(001)	2.5882	26.00	
AMC4	38.39	0.27	(111)	2.3429	31.16	
AMC4	44.66	0.28	(200)	2.0274	30.67	
AMC4	65.00	0.26	(220)	1.4337	36.23	

DENSIFICATION, POROSITY, AND MICRO-CT

The densification behavior and pore characteristics of the Al–3Mg–1Zn/ZrB_2–CeO_2 hybrid composites were evaluated to determine the influence of ceramic reinforcement content on consolidation efficiency and residual defect formation. Figure 14(a–d) presents the density, porosity, and micro-computed tomography (micro-CT) characteristics of the five compositions (AMC0–AMC4). The relative density gradually increased from AMC0 to AMC3. It decreased slightly at AMC4, indicating that densification is not a linear function of the reinforcement concentration. This behavior indicates that a moderate amount of ceramic may be useful for packing and squishing the powder, but a larger amount of reinforcement may cause differences in the material that prevent it from becoming denser. The trends were interpreted in connection with the reinforcement-distribution features observed under the microscope [24].

As shown in Fig. 14(a), the relative density increased from 92.1 ± 0.4% for AMC0 to 93.6 ± 0.3% for AMC1 and 95.0 ± 0.3% for AMC2, reaching a maximum of 96.2 ± 0.2% for AMC3 before decreasing slightly to 95.8 ± 0.3% for AMC4. The increase from AMC0 to AMC3 corresponds to 4.1 percentage points, equivalent to an approximately 4.5% relative improvement. These variations indicate that AMC3 achieved the highest relative density within the investigated composition range. The corresponding total porosity was estimated from the measured bulk density and the theoretical density of each composition using Eq. (3) [25].

$$P_{total}(\%) = \left(1 - \frac{\rho_{bulk}}{\rho_{theoretical}}\right) \times 100 = 100 - \rho_{relative}(\%) \quad (3)$$

*Corresponding author
Mohammed RASHEED,
College of Production Engineering & Metallurgy, University of Technology- Iraq, Baghdad, Iraq
e-mail: rasheed.mohammed40@yahoo.com

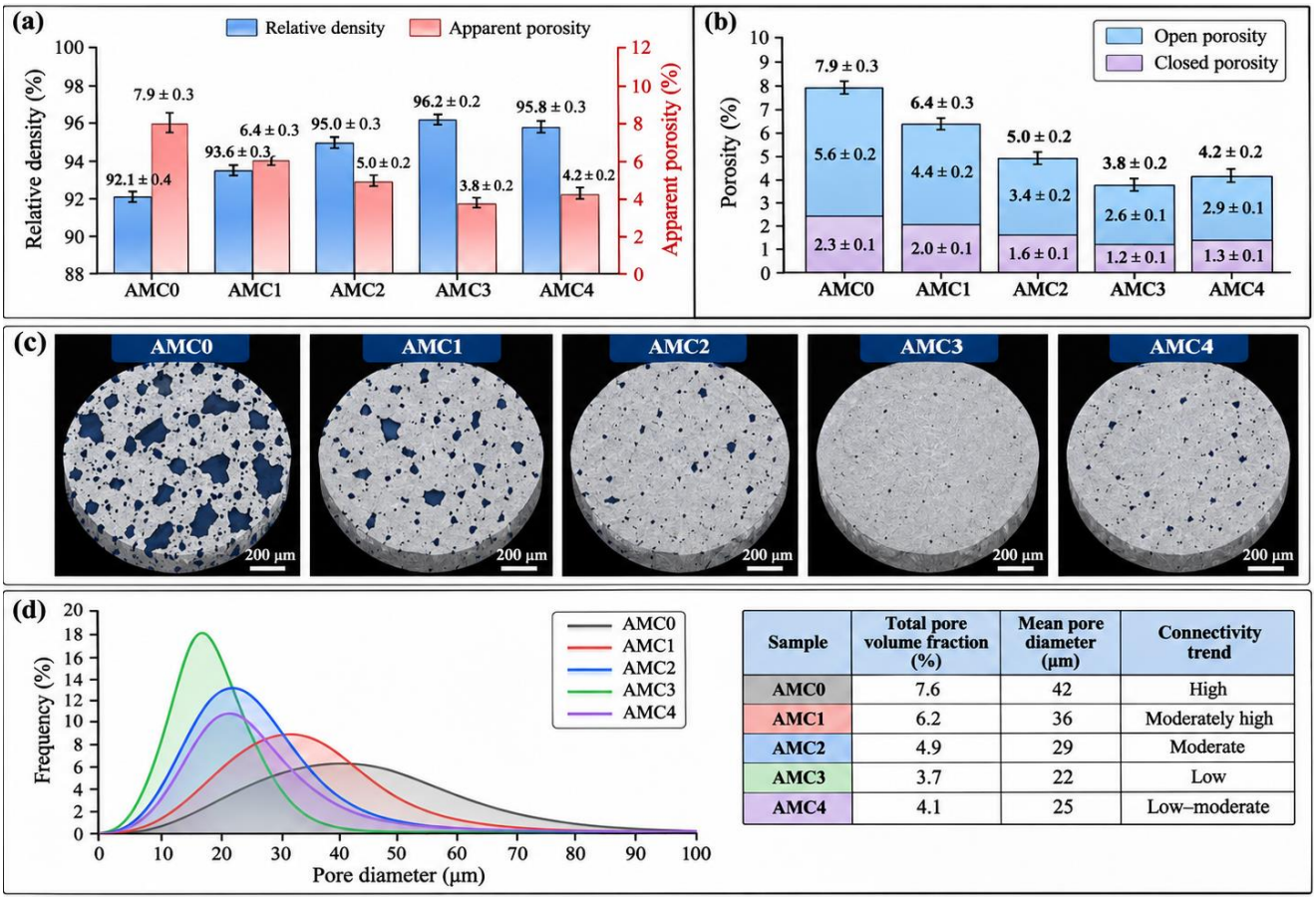
where (P_{total}) represents the total porosity (%), (ρ_{bulk}) is the experimentally determined bulk density ($g.cm^{-3}$), ($\rho_{theoretical}$) is the theoretical density calculated for each composite formulation ($g.cm^{-3}$), and ($\rho_{relative}$) denotes the relative density expressed as a percentage. The equation provides a density-derived estimate of total porosity and does not independently distinguish open from closed pores.

Based on Eq. (3), the calculated total porosity decreased from 7.9% for AMC0 to 6.4% for AMC1, 5.0% for AMC2, and a minimum of 3.8% for AMC3, followed by a slight increase to 4.2% for AMC4. This inverse relationship between relative density and total porosity reflects the corresponding reduction in residual void volume as densification increases. The relatively low total porosity of AMC3 indicates more effective consolidation within the investigated series, whereas the slight increase in AMC4 may be associated with reinforcement clustering or local differences in powder packing. These interpretations require evidence from microstructural and tomographic observations to be supported [25].

The contributions of the open- and closed-porosity shown in Fig. 14(b) provide us with more insight into the distribution of the remaining defects. The open porosity decreased from 5.6 ± 0.2% for AMC0 to 2.6 ± 0.1% for AMC3, while the closed porosity decreased from 2.3 ± 0.1% to 1.2 ± 0.1% over the same composition interval. For AMC4, the corresponding values increased slightly to 2.9 ± 0.1% and 1.3 ± 0.1%, respectively. Total porosity The reported central values of total porosity are consistent with the sum of these contributions. Less accessible pore volume may prevent electrolytes from being absorbed and less internal porosity may increase the strength of the structure. These effects must be correlated with the electrochemical and mechanical results [25].

The micro-CT characterization presented in Fig. 14(c,d) provides a complementary three-dimensional assessment of internal defects and pore morphology. This technique enables examination of pore distribution, connectivity, size, and spatial heterogeneity within the reconstructed specimen volume. When compared with bulk-density measurements, micro-CT can provide supporting evidence concerning isolated pore clusters and reinforcement-associated defects. However, quantitative micro-CT analysis depends on voxel size, image contrast, segmentation thresholds, and the minimum detectable pore dimensions. Consequently, comparisons between density-derived porosity and tomographic pore fractions must account for differences in measurement principles and spatial resolution [24, 25]

*Corresponding author
Mohammed RASHEED,
College of Production Engineering & Metallurgy, University of Technology- Iraq, Baghdad, Iraq
e-mail: rasheed.mohammed40@yahoo.com



Sample	Total pore volume fraction (%)	Mean pore diameter (μm)	Connectivity trend
AMC0	7.6	42	High
AMC1	6.2	36	Moderately high
AMC2	4.9	29	Moderate
AMC3	3.7	22	Low
AMC4	4.1	25	Low–moderate

Fig. 14. Densification and porosity characteristics of Al–3Mg–1Zn/ZrB_2–CeO_2 hybrid composites (AMC0–AMC4): (a) relative density and total porosity, (b) open- and closed-porosity fractions, and (c,d) three-dimensional micro-CT characterization of internal pore distributions.

Table 7 summarizes the experimentally determined relative density, calculated total porosity, and open- and closed-porosity fractions of the five Al–3Mg–1Zn/ZrB_2–CeO_2 hybrid composites (AMC0–AMC4), highlighting the influence of ceramic reinforcement content on densification behavior and residual pore characteristics.

Table 7. Relative density and porosity characteristics of Al–3Mg–1Zn/ZrB_2–CeO_2 hybrid composites (AMC0–AMC4).

Sample	Relative density (%)	Apparent porosity (%)	Open porosity (%)	Closed porosity (%)	Total pore volume fraction (%)	Mean pore diameter (μm)	Connectivity trend
AMC0	92.1 ± 0.4	7.9 ± 0.3	5.6 ± 0.2	2.3 ± 0.1	7.6	42	High
AMC1	93.6 ± 0.3	6.4 ± 0.3	4.4 ± 0.2	2.0 ± 0.1	6.2	36	Moderately high
AMC2	95.0 ± 0.3	5.0 ± 0.2	3.4 ± 0.2	1.6 ± 0.1	4.9	29	Moderate
AMC3	96.2 ± 0.2	3.8 ± 0.2	2.6 ± 0.1	1.2 ± 0.1	3.7	22	Low
AMC4	95.8 ± 0.3	4.2 ± 0.2	2.9 ± 0.1	1.3 ± 0.1	4.1	25	Low–moderate

VICKERS HARDNESS AND NANOINDENTATION

The mechanical properties of the Al–3Mg–1Zn/ZrB_2–CeO_2 hybrid composites were systematically evaluated using Vickers hardness testing and instrumented nanoindentation to determine the influence of ceramic reinforcement content on resistance to localized deformation. Figure 15(a–d) presents the Vickers

*Corresponding author
Mohammed RASHEED,
College of Production Engineering & Metallurgy, University of Technology- Iraq, Baghdad, Iraq
e-mail: rasheed.mohammed40@yahoo.com

hardness values, nanoindentation load–displacement curves, indentation hardness and reduced elastic modulus, and a schematic representation of the possible strengthening mechanisms, respectively. The combined measurements provide complementary information on the mechanical response of the five compositions (AMC0–AMC4), allowing the effects of ceramic loading, microstructural heterogeneity, and densification to be examined [26].

As shown in Fig. 15(a), the Vickers hardness increased progressively from 86 ± 3 HV0.5 for AMC0 to 95 ± 4 HV0.5 for AMC1 and 108 ± 4 HV0.5 for AMC2, reaching a maximum of 119 ± 5 HV0.5 for AMC3 before decreasing slightly to 113 ± 4 HV0.5 for AMC4. Compared with the unreinforced AMC0 composition, AMC3 exhibited an increase in Vickers hardness of approximately 38.4%. The improvement in hardness up to 3 wt.% reinforcement is consistent with greater resistance to localized plastic deformation, potentially arising from ceramic particle constraint, reinforcement–matrix interactions, and improved densification. The slight reduction in hardness for AMC4 may be related to increased reinforcement clustering and local microstructural heterogeneity [26].

Vickers hardness values were determined from the applied indentation force and the mean diagonal length of the residual impression

$$HV = 0.1891 \times \frac{F}{d^2} \quad (F\ in\ N;\ d\ in\ mm) \tag{4}$$

where (HV) is the Vickers hardness value, (F) is the applied force (N), and (d) is the arithmetic mean of the two indentation diagonals (mm). For the HV0.5 test condition, the load was maintained at 4.903 N. The reported hardness values were obtained from accurate indentation tests on properly prepared specimen surfaces.

The nanoindentation load-displacement curves in Fig. 15(b) exhibit that the five composite formulations behave differently in terms of localized deformation. All tests were performed with a diamond Berkovich indenter at a maximum indentation load of 5 mN. The maximum penetration depth decreased from ~730 nm for AMC0 to ~600 nm for AMC3, and then slightly increased to ~625 nm for AMC4. AMC3 has a smaller penetration depth at the same maximum load, and it is more difficult to dent. The differences in loading and unloading responses reflect composition-dependent variations in the elastic–plastic deformation behavior of the composites [27].

Instrumented indentation hardness was calculated from the maximum load applied and the projected area of contact (Eq. 5).

$$H_{IT} = \frac{P_{max}}{A_c} \tag{5}$$

where (H_{IT}) is the measured indentation hardness in Pa or GPa, (P_{max}) is the maximum indentation load in N, and (A_c) is the area that will be in contact with the load at its maximum point in m^2. The contact area was obtained from the calibrated indenter area function and the contact depth was obtained from the load-displacement response. The indentation hardness was measured using the Oliver-Pharr analysis method based on the unloading stiffness and the shape of the Berkovich indenter.

NANOINDENTATION HARDNESS AND REDUCED ELASTIC MODULUS

The nanoindentation results presented in Fig. 15(c) show indentation hardness values of 0.95, 1.10, 1.27, 1.40, and 1.32 GPa for AMC0, AMC1, AMC2, AMC3, and AMC4, respectively. The corresponding reduced elastic moduli were 70.2, 74.5, 79.3, 83.6, and 80.8 GPa. The indentation hardness was maximum and reduced modulus was minimum for AMC3 compared to AMC0. The values were increased by ~47.4% and ~19.1%, respectively. The results are in accordance with the Vickers hardness trend and some areas show an improvement in resistance to deformation at intermediate reinforcement content. The following decrease of AMC4 indicates that the addition of more ceramics does not always improve the mechanical performance under the conditions of the processing used [27].

*Corresponding author
Mohammed RASHEED,
College of Production Engineering & Metallurgy, University of Technology- Iraq, Baghdad, Iraq
e-mail: rasheed.mohammed40@yahoo.com

STRENGTHENING MECHANISMS

Figure 15(d) shows a simplified representation of the strengthening mechanisms that could have been responsible for the observed mechanical response. The addition of ZrB_2 and CeO_2 particles can increase the resistance of the material to plastic deformation by transferring load between the reinforcements and the matrix, blocking dislocation motion and limiting the local movement of the aluminum-based matrix. Contributions may be made by dislocation structures induced by particles and by resistance to grain boundary migration. But the relative importance of these mechanisms depends on the size of the reinforcements, their location, how they interact with the surface and how porous the material still is. In particular, as discussed in Section 3.3, the EBSD results show that AMC2 has the smallest average grain size and the highest hardness. Therefore, the higher hardness of AMC3 cannot be explained by the finer grain size alone, but densification and reinforcement effects should be considered [26].

INTEGRATED DISCUSSION

The results of Vickers hardness and nanoindentation show that AMC3 is the composition least susceptible to local deformation in the examined reinforcement range. This behavior is consistent with the highest relative density of 96.2% obtained for AMC3 in Section 3.5. Thus, the consolidation quality could be correlated with the observed mechanical improvement. AMC4 has a lower hardness and modulus despite the higher ceramic fraction. This demonstrates that the mechanical performance depends not only on the concentration of the reinforcement. Clearly, the correlation between the distribution of reinforcement, residual porosity and the indentation response demonstrates the necessity of considering a wide range of structural and mechanical parameters to design strengthening schemes for hybrid composites with aluminum matrix [27].

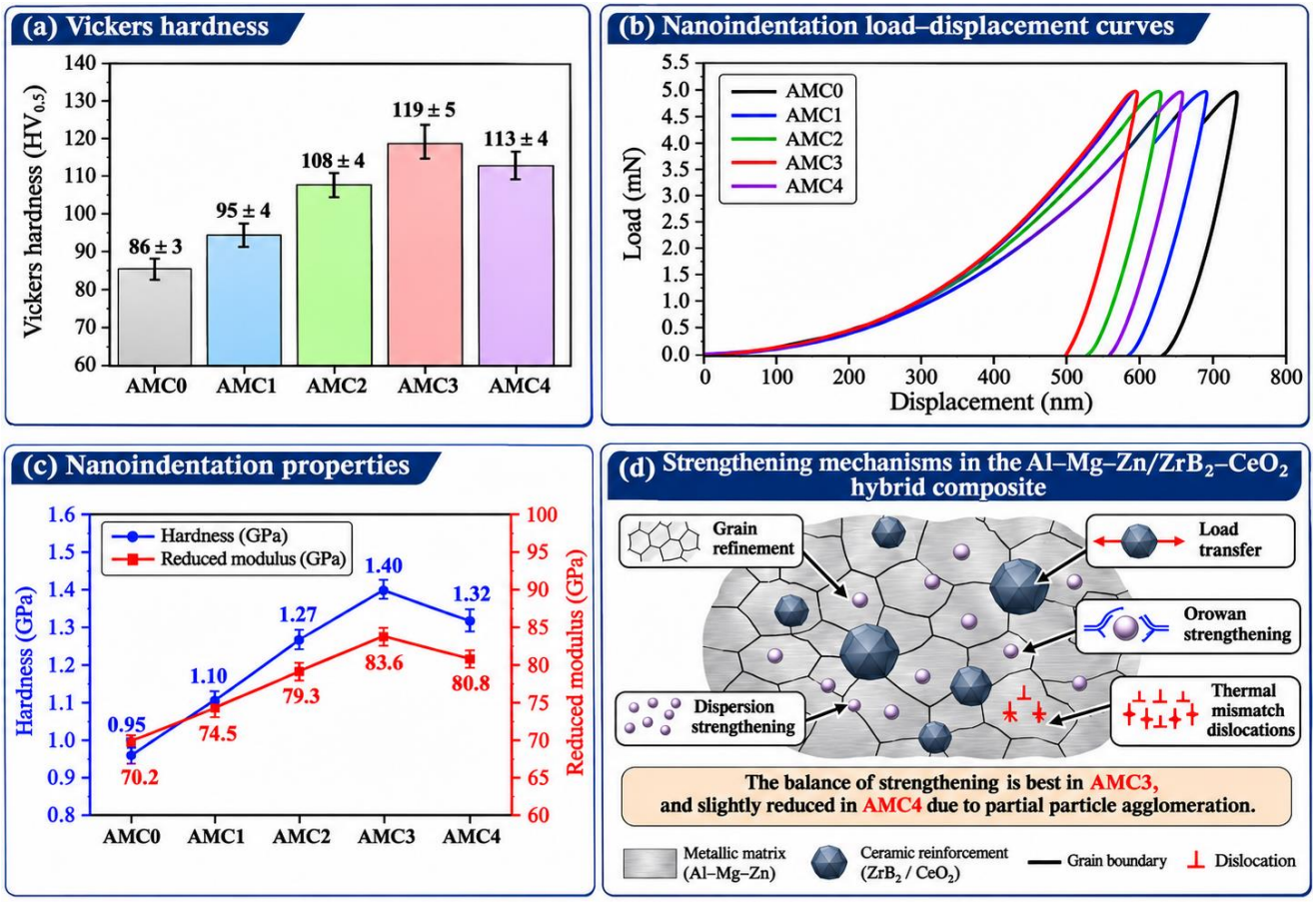


Fig. 15. Vickers hardness (HV0.5) and nanoindentation properties of Al–3Mg–1Zn/ZrB_2–CeO_2 hybrid composites (AMC0–AMC4): (a) Vickers hardness (HV0.5); (b) nanoindentation load–displacement curves at a maximum load of 5 mN; (c) indentation hardness and reduced elastic modulus; and (d) diagram of the proposed methods for improving the strength of the materials.

*Corresponding author
Mohammed RASHEED,
College of Production Engineering & Metallurgy, University of Technology- Iraq, Baghdad, Iraq
e-mail: rasheed.mohammed40@yahoo.com

Table 8 summarizes the Vickers hardness (HV0.5), instrumented nanoindentation hardness, reduced elastic modulus, and maximum indentation depth of the five Al–3Mg–1Zn/ZrB_2–CeO_2 hybrid composites (AMC0–AMC4), highlighting the influence of ceramic reinforcement content on localized mechanical deformation and indentation resistance.

Table 8. Vickers hardness, nanoindentation hardness, reduced elastic modulus, and maximum indentation depth of Al–3Mg–1Zn/ZrB_2–CeO_2 hybrid composites (AMC0–AMC4).

Sample	Vickers hardness (HV0.5)	Nanoindentation hardness (GPa)	Reduced modulus (GPa)	Max depth at 5 mN (nm)	Dominant interpretation
AMC0	86 ± 3	0.95	70.2	730	Baseline matrix response with limited obstacle density to dislocation motion.
AMC1	95 ± 4	1.10	74.5	690	Initial reinforcement addition improves load transfer and dispersion hardening.
AMC2	108 ± 4	1.27	79.3	640	Further strengthening due to higher particle density and stronger matrix constraint.
AMC3	119 ± 5	1.40	83.6	600	Optimum hybrid strengthening from balanced dispersion, grain refinement and Orowan-type resistance.
AMC4	113 ± 4	1.32	80.8	625	Slight decrease relative to AMC3 due to partial agglomeration and local heterogeneity.

TENSILE FLOW AND DUCTILITY

The tensile behavior of the Al–3Mg–1Zn/ZrB_2–CeO_2 hybrid composites was evaluated to investigate the influence of ceramic reinforcement content on yield strength, ultimate tensile strength (UTS), strain-hardening behavior, and ductility. Figure 16(a) presents the engineering stress–strain curves of the five composite formulations (AMC0–AMC4), while Fig. 16(b) compares their corresponding tensile properties. The stress–strain responses were characterized by an initial elastic region, followed by plastic deformation, strain hardening, and the attainment of maximum engineering stress before fracture. The differences among the five compositions provide a basis for examining reinforcement-dependent changes in load-bearing capacity and deformation behavior [28].

The engineering tensile stress was calculated by dividing the instantaneous applied tensile force by the original cross-sectional area of the specimen, as expressed in Eq. (6).

$$\sigma_{eng} = \frac{F}{A_0} \tag{6}$$

where σ_{eng} is the engineering tensile stress (MPa), F is the applied tensile force (N), and A_0 is the original cross-sectional area of the gauge section (mm^2). The use of force in newtons and area in square millimeters yields stress directly in MPa.

The corresponding engineering tensile strain was determined from the change in specimen gauge length relative to its initial value using Eqns. (7 and 8).

$$\varepsilon_{ebg} = \frac{\Delta L}{L_0} = \frac{L - L_0}{L_0} \tag{7}$$

$$\varepsilon_{eng} = \frac{\Delta L}{L_o} = \frac{L - L_o}{L_o} \tag{8}$$

*Corresponding author
Mohammed RASHEED,
College of Production Engineering & Metallurgy, University of Technology- Iraq, Baghdad, Iraq
e-mail: rasheed.mohammed40@yahoo.com

where ε_{eng} is engineering tensile strain (dimensionless), ΔL is the change in gauge length (mm), L_o is the original gauge length (mm), and L is the instantaneous gauge length during tensile loading (mm). The recorded force and strain data were used to construct Fig. 16(a).

The ultimate tensile strength was determined from the maximum engineering tensile stress reached during testing, as defined in Eq. (9).

$$UTS = \frac{F_{max}}{A_o} \tag{9}$$

where UTS is the ultimate tensile strength (MPa), F_{max} is the maximum tensile force recorded during the test (N), and A_o is the original cross-sectional area of the gauge section (mm^2).

The 0.2% offset yield strength was determined from the intersection of the engineering stress–strain curve with a line parallel to the initial linear elastic region and displaced by an engineering strain of 0.002. The equation describing this offset line is given in Eq. (10).

$$\sigma_{offset} = E(\varepsilon_{eng} - 0.002) \tag{10}$$

where σ_{offset} is the stress corresponding to the 0.2% offset line (MPa), E is Young's modulus derived from the initial elastic region (MPa), ε_{eng} is engineering tensile strain, and 0.002 is the specified strain offset. The yield strength ($YS_{0.2}$) is the stress at the intersection of the measured stress–strain curve and this offset line.

The results of the tensile test are shown in Table 9. The 0.2% offset yield strength increased from 160 MPa for AMC0 to 185 MPa for AMC1 and 210 MPa for AMC2. It reached a maximum of 235 MPa for AMC3 and then dropped slightly to 228 MPa for AMC4. The same thing happened to UTS. It increased from 250 MPa for AMC0 to 285 MPa for AMC1 and 320 MPa for AMC2 and reached a high of 350 MPa for AMC3 and decreased to 340 MPa for AMC4. Results show that AMC3 is the composition with highest UTS and yield strength in the range of reinforcements studied. The small drop in both parameters for AMC4 indicates that addition of more ceramic reinforcement above 3 wt.% did not make the material stronger in the tensile test [28].

The ductility decreased gradually with increase in tensile strength. Elongation at fracture decreased from 16.5% for AMC0 to 15.0%, 13.5%, 12.0%, and 10.5% for AMC1, AMC2, AMC3, and AMC4, respectively. When determined from original and final gauge lengths measured after fracture, percentage elongation was calculated using Eq. (10).

$$EL\ (\%) = \frac{L_f - L_o}{L_o} \times 100$$

where EL is the elongation after fracture in %, Lf is the gage length measured after the two halves of the broken specimen are carefully joined back together in mm, and L_0 is the gage length before the break. When elongation is obtained directly from a calibrated extensometer at fracture, the corresponding measurement definition must be specified.

To quantify the influence of ceramic reinforcement content relative to the unreinforced AMC0 composition, the percentage change in yield strength was calculated using Eq. (11).

$$\Delta YS\ (\%) = \frac{YS_i - YS_{AMC0}}{YS_{AMC0}} \times 100 \tag{11}$$

where ΔYS is percentage yield-strength change, YS_i is the 0.2% offset yield strength of a given composition (MPa), and YS_{AMC0} is the corresponding yield strength of the unreinforced AMC0 reference (MPa).

Similarly, the percentage change in ultimate tensile strength relative to AMC0 was calculated using Eq. (12).

*Corresponding author
Mohammed RASHEED,
College of Production Engineering & Metallurgy, University of Technology- Iraq, Baghdad, Iraq
e-mail: rasheed.mohammed40@yahoo.com

$$\Delta UTS\ (\%) = \frac{UTS_{\mathrm{i}} - UTS_{\mathrm{am}}c_0}{UTS_{\mathrm{am}}c_0} \times 100 \quad (12)$$

where ΔUTS is percentage ultimate-tensile-strength change, UTS_i is the ultimate tensile strength of a given composition (MPa), and UTS_{AMC0} is the corresponding UTS of the AMC0 reference (MPa).

According to Eqns. (11) and (12), percentage increases in yield strength relative to AMC0 were 15.6%, 31.3%, 46.9%, and 42.5% for AMC1, AMC2, AMC3, and AMC4, respectively. Corresponding UTS increases were 14.0%, 28.0%, 40.0%, and 36.0%. AMC3 showed the largest response to strengthening in terms of drop in elongation (27.3% drop compared to AMC0), while AMC4 showed 36.4% drop in elongation. Table 9 shows the strength-ductility trade-off for different level of reinforcement [28].

Some of the reasons that may have contributed to the increase in strength are matrix constraint due to reinforcement, efficient load transfer at the interface, limited dislocation motion and variation in the quality of consolidation. More reinforcement can cause a clumping of particles, different forms of strain build up and local damage which reduces the flexibility of the material. You cannot just compare tensile properties to work out how important each of these mechanisms is; you also need to look at microstructural and fracture-surface evidence [28].

As mentioned in Section 3.5, the highest strength found in AMC3 correlates with its reported relative density of 96.2%, which was higher than that of AMC0 (92.1%). Nevertheless, the EBSD descriptors introduced in Section 3.3 reveal that AMC2 has the lowest average grain diameter. Therefore, the high tensile strength claimed for AMC3 cannot be solely attributed to finer grains; densification, reinforcement distribution, interface properties, and damage sensitivity also play a role [28].

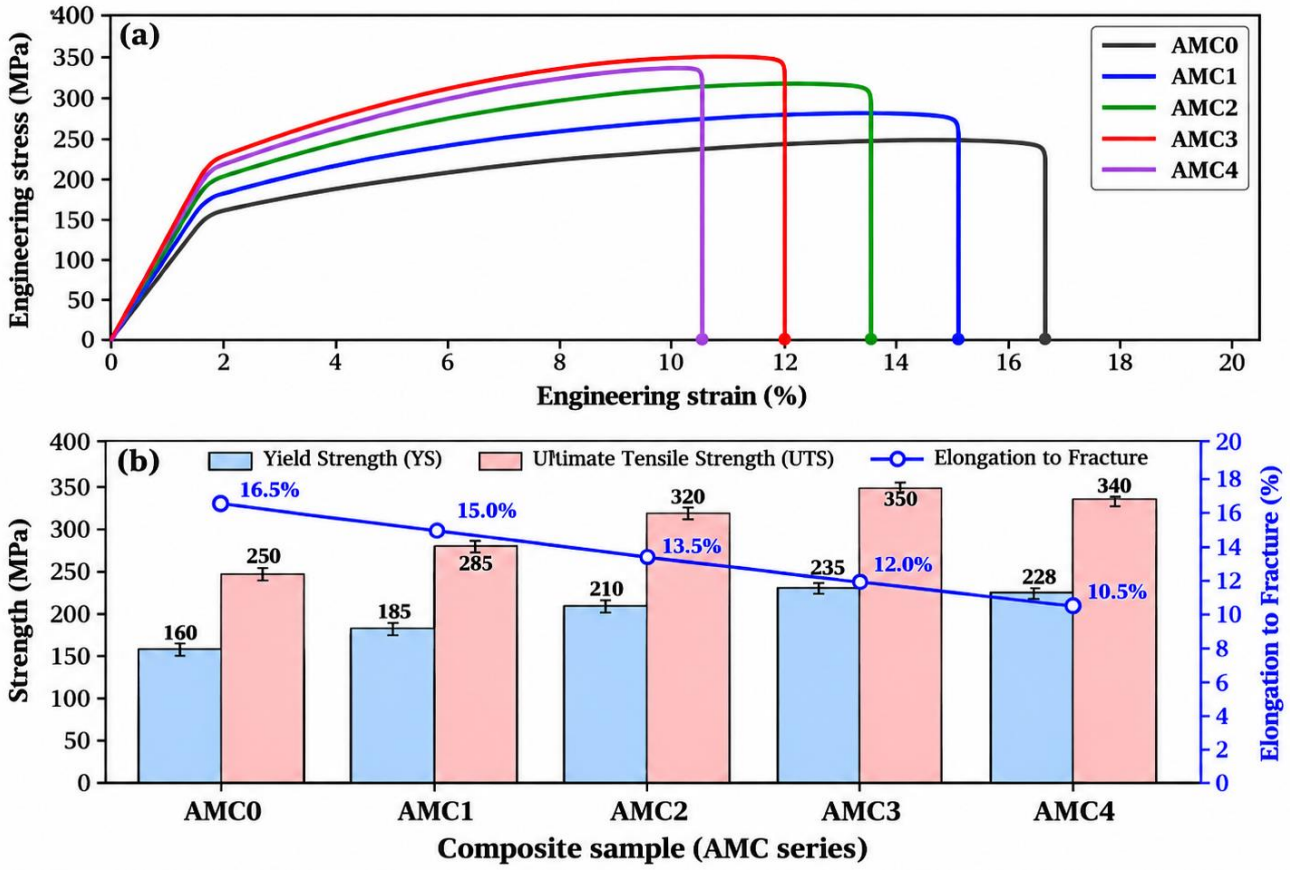


Fig. 16. Tensile behavior of Al–3Mg–1Zn/ZrB_2–CeO_2 hybrid composites (AMC0–AMC4): (a) engineering stress–strain curves and (b) comparison of 0.2% offset yield strength, ultimate tensile strength, and elongation at fracture.

*Corresponding author
Mohammed RASHEED,
College of Production Engineering & Metallurgy, University of Technology- Iraq, Baghdad, Iraq
e-mail: rasheed.mohammed40@yahoo.com

Table 9 summarizes the 0.2% offset yield strength, ultimate tensile strength (UTS), and elongation at fracture of the five Al–3Mg–1Zn/ZrB_2–CeO_2 hybrid composites (AMC0–AMC4), highlighting the influence of ceramic reinforcement content on tensile strength, ductility, and overall mechanical performance.

Table 9. Tensile properties of Al–3Mg–1Zn/ZrB_2–CeO_2 hybrid composites (AMC0–AMC4), including 0.2% offset yield strength, ultimate tensile strength, elongation at fracture, and percentage changes in yield strength and ultimate tensile strength relative to AMC0.

Sample	Yield strength (MPa)	UTS (MPa)	Elongation at fracture (%)	YS change vs AMC0 (%)	UTS change vs AMC0 (%)
AMC0	160	250	16.5	0.0	0.0
AMC1	185	285	15.0	+15.6	+14.0
AMC2	210	320	13.5	+31.3	+28.0
AMC3	235	350	12.0	+46.9	+40.0
AMC4	228	340	10.5	+42.5	+36.0

COMPRESSION AND ABSORBED DEFORMATION WORK

The deformation behavior of Al–3Mg–1Zn/ZrB_2–CeO_2 hybrid composites under compression was studied to examine the influence of the amount of ceramic reinforcement on yield strength, peak compressive stress, strain-hardening response, and deformation-energy absorption. The engineering compressive stress–strain curves, the corresponding compressive strength parameters and the energy-absorption properties of the five compositions (AMC0–AMC4) are shown in Figure 17(a–c). The same specimen shape, loading conditions and strain definitions were used to investigate the compression responses and to compare the mechanical behavior dependent on reinforcement. The influence of ceramic dispersion and residual porosity on resistance to deformation under compression was studied in detail [29].

The engineering compressive stress is calculated by dividing the applied compressive force by the original cross-sectional area of each specimen as shown in Eq. (13).

$$\sigma_c = \frac{F_c}{A_o} \tag{13}$$

where (σ_c) is the engineering compressive stress in MPa, (Fc) is the compressive force applied in N and (A_o) is the cross-sectional area that was not loaded (in mm^2). Positive amount of compressive stress is reported in this article.

The corresponding engineering compressive strain was determined from the reduction in specimen height relative to its original height using Eq. (14).

$$\varepsilon_c = \frac{h_o - h}{h_o} = \frac{\Delta L}{h_o} \tag{14}$$

where (ε_c) is the engineering compressive strain (dimensionless), (h_0) is the original specimen height (mm), (h) is the instantaneous height during compression (mm), and (Δh) is the reduction in specimen height (mm). The strain definition represents compression as a positive quantity.

Figure 17(b) shows the compressive strength characteristics. The compressive yield strength was increased from 198 MPa for AMC0 to 222 MPa for AMC1 and 240 MPa for AMC2. It reached a maximum of 268 MPa for AMC3 and then decreased slightly to 260 MPa for AMC4. The increase of yield strength of AMC3 was about 35.4% compared to AMC0. The maximum compressive stress was comparable. It increased from 300 MPa for AMC0 to 341 MPa for AMC1, 381 MPa for AMC2 and a maximum of 439 MPa for AMC3, before dropping to 422 MPa for AMC4. The peak compressive stress of AMC3 was approximately 46.3% higher than that of the composition without reinforcement. AMC3 is the mixture with the best compressive resistance of the five combinations from these tests [29].

*Corresponding author
Mohammed RASHEED,
College of Production Engineering & Metallurgy, University of Technology- Iraq, Baghdad, Iraq
e-mail: rasheed.mohammed40@yahoo.com

Fig. 17(a) shows the engineering compressive stress-strain curves that offer more insights into the material deformation as the compressive load increases. The reinforced compositions have higher stresses than AMC0 in the same range of strains, which means that they are less likely to be deformed when compressed. The response that was seen may have something to do with the way the ceramic reinforcements carry weight and the way the metal matrix limits how much it can bend. However, specimen geometry, friction on the platens, barreling and localized deformation can all alter the behavior of compression. Thus, for the purpose of comparison of compressive strength and strain hardening characteristics, the specimens need to be prepared and tested in the same way every time [29].

The energy absorbed per unit of the initial specimen volume during compressive deformation was calculated by integrating the engineering compressive stress–strain curve until a certain strain limit, as shown in Equation (15).

$$W_v(\varepsilon_{max}) = \int_0^{\varepsilon_{max}} \sigma_c(\varepsilon_c)\, d\varepsilon_c \quad (15)$$

where Wv is the absorbed deformation energy per unit initial specimen volume. σ_c is the engineering compressive stress in MPa, ε_c is the engineering compressive strain and ε_{max} is the selected upper strain limit. Strain is dimensionless so that the integral of stress in MPa yields an energy density of $MJ.m^{-3}$. To be fair, the same limit of integration has to be used for all the five compositions.

The energy absorption properties were examined from below the corresponding engineering stress-strain curves to a common maximum strain as shown in Fig. 17(c). The deformation energy absorbed was higher when the integrated compressive stress over the deformation interval chosen was higher. Thus the meaning of this parameter is related to the whole shape of the curve and not only to the peak compressive stress. The relationship between reinforcement content and absorbed energy was considered alongside the measured yield strength, peak compressive stress, and deformation characteristics of the composites [29].

The highest compressive yield and peak stress values were associated with AMC3, consistent with its comparatively high relative density and low residual porosity discussed in Section 3.5. Improved consolidation can reduce internal stress concentrations and contribute to more effective resistance against compressive deformation. The subsequent decrease in compressive strength for AMC4 may be associated with reinforcement clustering, changes in interfacial characteristics, or localized microstructural heterogeneity [29].

*Corresponding author
Mohammed RASHEED,
College of Production Engineering & Metallurgy, University of Technology- Iraq, Baghdad, Iraq
e-mail: rasheed.mohammed40@yahoo.com

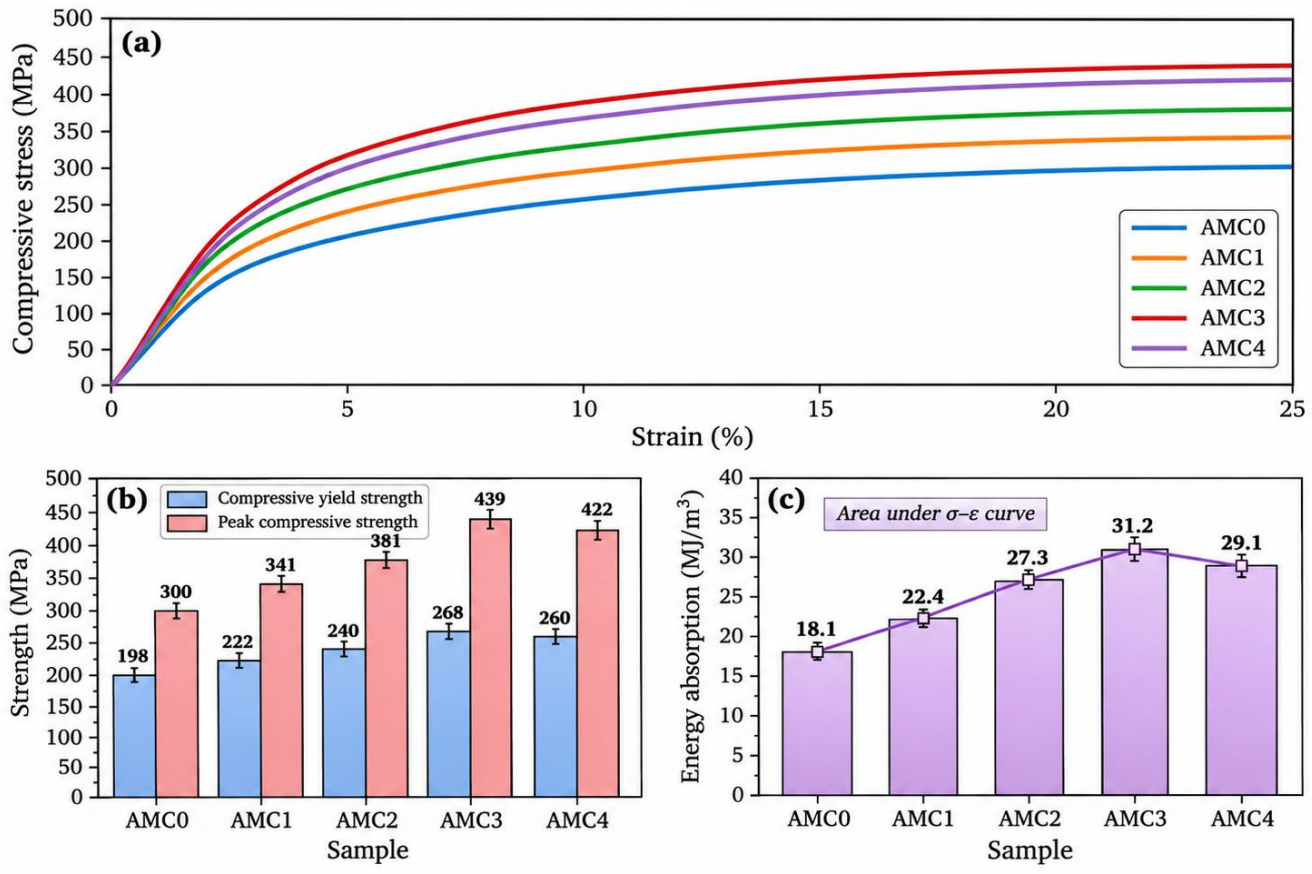


Fig. 17. Compressive mechanical behavior of Al–3Mg–1Zn/ZrB_2–CeO_2 hybrid composites (AMC0–AMC4): (a) engineering compressive stress–strain curves, (b) compressive yield strength and peak compressive stress, and (c) absorbed deformation energy per unit volume.

Table 10 summarizes the compressive yield strength, peak compressive stress, and absorbed deformation energy per unit volume of the five Al–3Mg–1Zn/ZrB_2–CeO_2 hybrid composites (AMC0–AMC4).

Table 10. Compressive yield strength, peak compressive stress, and absorbed deformation energy of Al–3Mg–1Zn/ZrB_2–CeO_2 hybrid composites (AMC0–AMC4).

Sample	Yield strength (MPa)	Peak strength (MPa)	Examined energy indicator ($MJ.m^{-3}$)	Change in peak strength vs AMC0 (%)
AMC0	198	300	18.1	0.0
AMC1	222	341	22.4	13.7
AMC2	240	381	27.3	27.0
AMC3	268	439	31.2	46.3
AMC4	260	422	29.1	40.7

OPEN-CIRCUIT POTENTIAL (OCP) AND POTENTIODYNAMIC POLARIZATION (TAFEL)

The electrochemical response of the Al–3Mg–1Zn/ZrB_2–CeO_2 hybrid composites (AMC0–AMC4) was assessed through open-circuit potential (OCP) monitoring and potentiodynamic polarization in 3.5 wt.% NaCl at 25 ± 1 °C. The specimens were tested in a conventional three-electrode cell using an Ag/AgCl reference electrode, a platinum counter electrode, and an exposed working-electrode area of 1 cm^2. Figure 18 presents the OCP–time responses, whereas Fig. 19 presents the polarization behavior of the five compositions. Because OCP is a mixed potential and polarization provides current-dependent kinetic

*Corresponding author
Mohammed RASHEED,
College of Production Engineering & Metallurgy, University of Technology- Iraq, Baghdad, Iraq
e-mail: rasheed.mohammed40@yahoo.com

information, the two measurements were interpreted as complementary rather than interchangeable indicators of corrosion behavior [30].

The OCP profiles shown in Fig. 18 evolved toward less negative potentials and approached a quasi-stable region during the 3600 s observation interval. The reported final OCP values were −0.931, −0.758, −0.643, −0.523, and −0.557 V versus Ag/AgCl for AMC0, AMC1, AMC2, AMC3, and AMC4, respectively. AMC3 exhibited the most positive final OCP, followed by AMC4, AMC2, AMC1, and AMC0. The positive shift of the final OCP relative to AMC0 was calculated using Eq. (16); this shift reflects a change in the mixed interfacial potential and does not, by itself, quantify corrosion resistance [30].

$$\Delta E_{(}OCP,j_{)} = E_{(}OCP,j_{)} - E_{(}OCP,AMC0_{)} \quad (16)$$

where $\Delta E_{(}OCP,j_{)}$ is the difference in final OCP between composition j and AMC0 (V); $E_{(}OCP,j_{)}$ is the final open-circuit potential of the investigated composition (V versus Ag/AgCl); and $E_{(}OCP,AMC0_{)}$ is the corresponding final OCP of the unreinforced reference specimen.

Applying Eq. (16) to the listed values gives a +0.408 V shift for AMC3 relative to AMC0, whereas AMC4 is 0.034 V more negative than AMC3. This difference identifies AMC3 as the most positive OCP response within the dataset, but any inference about corrosion kinetics requires the polarization-current measurements discussed below [30].

The potentiodynamic polarization curves in Fig. 19 compare the anodic and cathodic electrochemical responses over a common potential range. Current was normalized by the exposed specimen area to obtain current density ($A.cm^{-2}$). Suitable charge-transfer-controlled sections of each branch may be described by the Tafel relationship given in Eq. (17), provided that linear regions exist when potential is plotted against the logarithm of current density. Anodic and cathodic branches must be fitted independently; extrapolation should not be applied indiscriminately to passive, diffusion-limited, or pitting-affected regions [30].

$$\eta = a + b\,log_{10}(|i|) \quad (17)$$

the electrode overpotential (V) is given by $\eta = E - E_{corr}$. E is the applied electrode potential (V versus Ag/AgCl) and E corr is the corrosion potential (V versus Ag/AgCl). The Tafel intercept (V), the signed Tafel slope ($V.dec^{-2}$), and the current density ($A.cm^{-2}$) are also given. A numerical value of the current density is used to evaluate the logarithm relative to a standard reference unit. The intersection of valid anodic and cathodic branches extrapolated separately provides estimates of E_{corr} and i_{corr}.

The corrosion current densities listed for AMC0–AMC4 are 4.6×10^{-5}, 3.2×10^{-6}, 7.9×10^{-7}, 1.9×10^{-7}, and 3.1×10^{-7} A cm^{-2}, respectively. AMC3 has the lowest value and the slightly higher value of AMC4 is due to its higher nominal ceramic content. The lower i_{corr} value of AMC3 is in line with the assumptions of a valid Tafel analysis. Thus, the estimated uniform-corrosion current will be lower under the stated test conditions. A separate test is required before any conclusions can be drawn on pitting resistance or long term exposure behavior [30,31].

To allow numerical comparison with the AMC0 reference composition, the percentage decrease in corrosion current density was calculated using Eq. (18) [30].

$$R_{(}i_{)}\,(\%) = [(i_{(}corr,AMC0_{)} - i_{(}corr,j_{)})/i_{(}corr,AMC0_{)}] \times 100 \quad (18)$$

where $R_{(}i_{)}$ is the percentage reduction in corrosion current density relative to AMC0 (%), $i_{(}corr,AMC0_{)}$ is the corrosion current density of AMC0 ($A.cm^{-2}$), and $i_{(}corr,j_{)}$ is the corresponding corrosion current density of composition j ($A.cm^{-2}$). This relative comparison should be used only when the quantities are extracted by comparable polarization-analysis procedures.

Using Eq. (18), the listed AMC3 current density corresponds to a reduction of approximately 99.59% relative to AMC0, or a ratio of approximately 242:1. This numerical comparison is valid for the supplied current-density values but does not independently verify their experimental origin. Corrosion current

*Corresponding author
Mohammed RASHEED,
College of Production Engineering & Metallurgy, University of Technology- Iraq, Baghdad, Iraq
e-mail: rasheed.mohammed40@yahoo.com

densities should be reproduced by the measured Fig. 19 polarization traces and associated fitting records before any reduction factor is claimed as an experimental result [30].

Potential for open circuits and potential for corrosion were considered as separate outputs. The first one is obtained from the potential-time trace without any outside polarization . The second one is obtained from the potentiodynamic response . The earlier figure and table give identical numbers for each composition for the final OCP and E_{corr}.

The electrochemical response differences may be due to the differences in porosity, reinforcement dispersion, matrix continuity, and surface-film chemistry. The derived porosity for the higher density and lower density to AMC3 in Section 3.5 is consistent with fewer accessible defects. However, changes in oxide chemistry, local galvanic coupling, and film stability could still be counteracting factors [30].

The final OCP values and polarization derived corrosion parameters for AMC0–AMC4 are presented in Table 11. The values are given separately for each measurement method. It is important to use the comparison to find the lowest listed corrosion current density for AMC3 under the given conditions. The electrochemical interpretation must also be consistent with the actual curve fits, residual porosity, reinforcement distribution and oxide-film evidence.

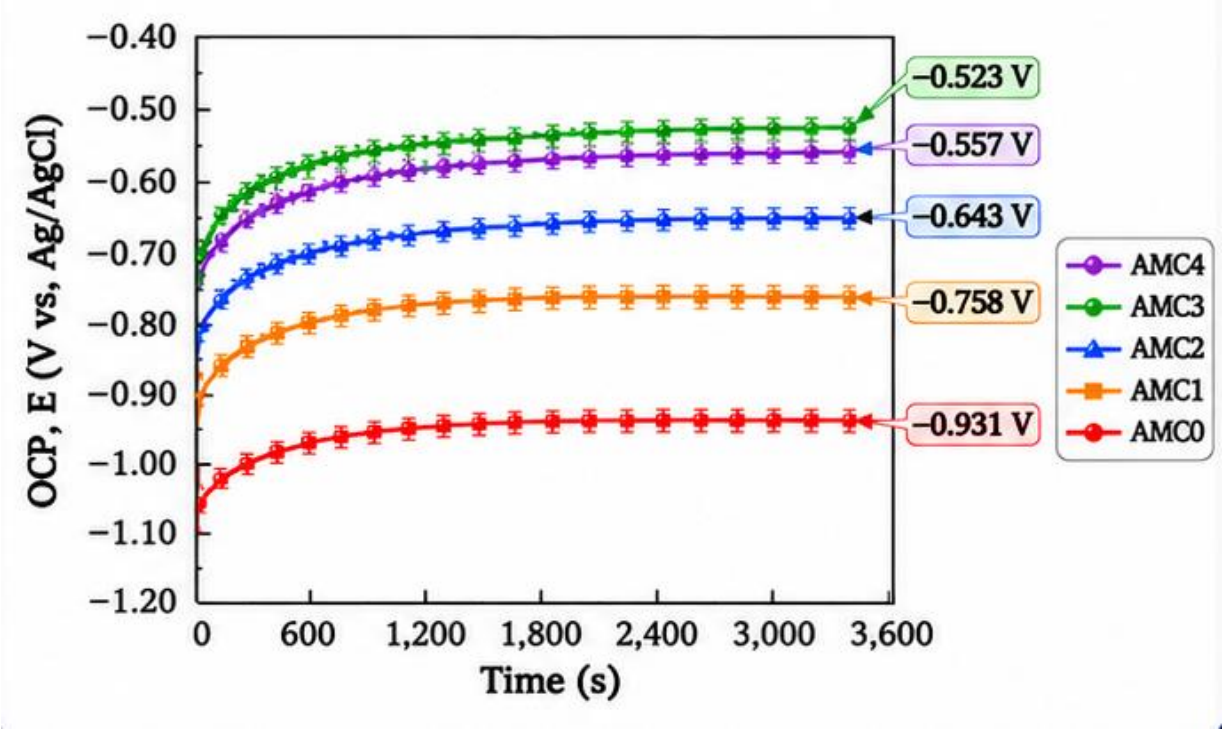


Fig. 18. Open-circuit potential (OCP) evolution of Al–3Mg–1Zn/ZrB_2–CeO_2 hybrid composites (AMC0–AMC4) during 3600 s immersion in 3.5 wt.% NaCl solution, measured relative to an Ag/AgCl reference electrode.

*Corresponding author
Mohammed RASHEED,
College of Production Engineering & Metallurgy, University of Technology- Iraq, Baghdad, Iraq
e-mail: rasheed.mohammed40@yahoo.com

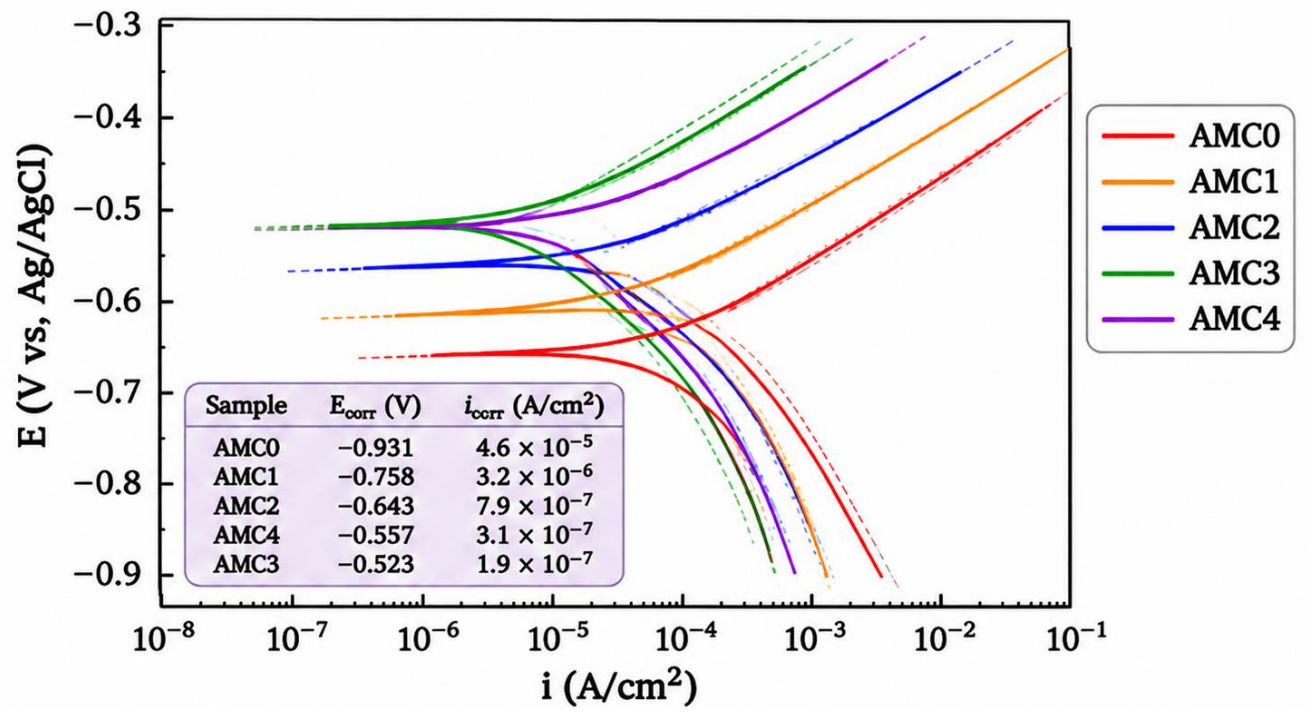


Fig. 19. Potentiodynamic polarization curves of Al–3Mg–1Zn/ZrB_2–CeO_2 hybrid composites (AMC0–AMC4) in 3.5 wt.% NaCl solution, showing the electrochemical responses used to determine corrosion potential and corrosion current density.

Table 11. Open-circuit potential, corrosion potential, corrosion current density, and electrochemical polarization parameters of Al–3Mg–1Zn/ZrB_2–CeO_2 hybrid composites (AMC0–AMC4).

Sample	OCP (V vs. Ag/AgCl)	E_{corr} (V vs. Ag/AgCl)	i_{corr} ($A.cm^{-2}$)
AMC0	−0.931	−0.931	4.6×10^{-5}
AMC1	−0.758	−0.758	3.2×10^{-6}
AMC2	−0.643	−0.643	7.9×10^{-7}
AMC3	−0.523	−0.523	1.9×10^{-7}
AMC4	−0.557	−0.557	3.1×10^{-7}

CONCLUSIONS

In the present study, influence of adding a hybrid ZrB_2-CeO_2 reinforcement on microstructure, densification, mechanical strength and electrochemical response of powder-metallurgy Al-3Mg-1Zn composites was studied. Five compositions (AMC0–AMC4), containing 0–4 wt.% total ceramic reinforcement at a fixed ZrB_2:CeO_2 mass ratio of 3:1, were systematically examined using complementary structural, morphological, mechanical, and electrochemical characterization techniques. The combined analysis showed that differences in composition influence the distribution of reinforcements, the characteristics of grains, the amount of residual porosity, the resistance to deformation and the behavior of polarization, which shows the importance of controlling ceramic loading and consolidation quality in aluminum-based hybrid composites.

The densification results showed that AMC3 had the highest relative density of 96.2% compared to the unreinforced AMC0 specimen with a relative density of 92.1%. The total porosity according to density decreased from 7.9% to 3.8% indicating a better material consolidation at an intermediate content of reinforcement. When the ceramic fraction was increased to 4 wt.%, the relative density slightly decreased to 95.8% and the total porosity increased to 4.2%. The location of the ceramic-rich areas and the location of the

*Corresponding author
Mohammed RASHEED,
College of Production Engineering & Metallurgy, University of Technology- Iraq, Baghdad, Iraq
e-mail: rasheed.mohammed40@yahoo.com

different shapes and sizes of the particles were further investigated by the FESEM–EDS observations and microstructural characterization. The results indicate that the response to densification is not only a function of the amount of reinforcement used, but also of how the powder is packed, the distribution of particles and whether any defects are left after processing.

The mechanical testing results indicated significant enhancement in hardness and strength with increasing reinforcement content up to AMC3. The Vickers hardness increased from AMC0 with 86 HV0.5 to AMC3 with 119 HV0.5, an improvement of ~ 38.4 %. The reduced elastic modulus increased from 70.2 GPa to 83.6 GPa and the nanoindentation hardness increased from 0.95 GPa to 1.40 GPa. The ultimate tensile strength went up from 250 MPa to 350 MPa and the 0.2% offset tensile yield strength went up from 160 MPa to 235 MPa. These are increases of around 46.9% and 40.0% respectively. The maximum compressive stress also increased from 300 MPa to 439 MPa, which is an increase of about 46.3%. These improvements resulted in a reduction of tensile elongation from 16.5% to 12.0%, which suggests a trade-off between strength and ductility. The corresponding reduction in hardness and strength of AMC4 indicates that increasing ceramic loading does not necessarily provide further mechanical benefits.

Crystallographic analysis showed that the reinforcement content and grain structure could be related in more than one way. EBSD analysis revealed that AMC2 had the lowest average diameter of the aluminum-matrix grains (2.2 μm) and the lowest average misorientation of the kernels (1.11°). AMC3 had a higher average grain diameter (2.9 μm) and a higher average KAM (1.58°). Thus, the better mechanical response of AMC3 cannot be explained only by grain refinement. Instead, you need to think about how densification, matrix-related reinforcement constraint, interfacial load transfer, and other microstructural factors affect the whole. The XRD analysis showed the main α-Al reflections and provided phase-related information that helped to understand the ceramic additives. The results show that the same amount of reinforcement does not always lead to the best microstructural improvement and overall mechanical strengthening.

Electrochemical tests revealed that the compositions studied showed large differences in the open-circuit potential and in the polarization derived corrosion current density. The OCP finally shifted from -0.931 V for AMC0 to -0.523 V for AMC3 vs. Ag/AgCl, which is a difference of 0.408 V in favor of AMC3. The corrosion current density was reduced from 4.6×10^{-5} A.cm^{-2} for AMC0 to 1.9×10^{-7} A.cm^{-2} for AMC3, which is a reduction of ~99.6% under the studied conditions. The OCP of AMC4 is slightly lower and the corrosion current density is higher than AMC3, which indicated that increasing the reinforcement content would not improve these electrochemical indicators. The observed response may be related to variations in consolidation quality, number of open pores, distribution of reinforcement and properties of the surface sample, but the relative roles of these factors need to be confirmed by separate mechanistic testing.

REFERENCES

[1] P. Samal, P. R. Vundavilli, A. Meher, and M. M. Mahapatra, “Recent progress in aluminum metal matrix composites: A review on processing, mechanical and wear properties,” Journal of Manufacturing Processes, vol. 59, pp. 131–152, 2020, doi: https://doi.org/10.1016/j.jmapro.2020.09.010.
[2] D. Akgümüş Gök, C. Bayraktar, and M. Hoşkun, “A review on processing, mechanical and wear properties of Al matrix composites reinforced with Al2O3, SiC, B4C and MgO by powder metallurgy method,” Journal of Materials Research and Technology, 2024, doi: https://doi.org/10.1016/j.jmrt.2024.06.110.
[3] C. Suryanarayana, “Mechanical alloying and milling,” Progress in Materials Science, vol. 46, nos. 1–2, pp. 1–184, 2001, doi: https://doi.org/10.1016/S0079-6425(99)00010-9.
[4] Y. Liu et al., “Microstructure and mechanical properties of Al matrix composites produced by Al–CeO_2 in-situ reaction,” Materials Characterization, 2025, doi: https://doi.org/10.1016/j.matchar.2025.115373.
[5] G. Chen, J. Wan, N. He, H. Zhang, F. Han, and Y. Zhang, “Strengthening mechanisms based on reinforcement distribution uniformity for particle reinforced aluminum matrix composites,” Transactions of

*Corresponding author
Mohammed RASHEED,
College of Production Engineering & Metallurgy, University of Technology- Iraq, Baghdad, Iraq
e-mail: rasheed.mohammed40@yahoo.com

Nonferrous Metals Society of China, vol. 28, no. 12, pp. 2395–2400, 2018, doi: https://doi.org/10.1016/S1003-6326(18)64885-X.
[6] C. S. Kim, K. Cho, M. H. Manjili, and M. Nezafati, "Mechanical performance of particulate-reinforced Al metal-matrix composites (MMCs) and Al metal-matrix nano-composites (MMNCs)," Journal of Materials Science, vol. 52, pp. 13319–13349, 2017, doi: https://doi.org/10.1007/s10853-017-1378-x.
[7] P. M. Mathebula, P. Sarmah, and K. Gupta, "Fabrication and metallurgical characterization of hybrid al matrix composites reinforced with SiC and Al2O3 using powder metallurgy," The International Journal of Advanced Manufacturing Technology, 2026, doi: https://doi.org/10.1007/s00170-026-17757-8.
[8] W. C. Oliver and G. M. Pharr, "An improved technique for determining hardness and elastic modulus using load and displacement sensing indentation experiments," Journal of Materials Research, vol. 7, no. 6, pp. 1564–1583, 1992, doi: https://doi.org/10.1557/JMR.1992.1564.
[9] Y. Shadangi, K. Chattopadhyay, and N. K. Mukhopadhyay, "Powder metallurgical processing of Al matrix composite reinforced with AlSiCrMnFeNiCu high-entropy alloys: Microstructure, thermal stability, and microhardness," Journal of Materials Research, vol. 38, pp. 248–264, 2023, doi: https://doi.org/10.1557/s43578-022-00866-x.
[10] A. Wąsik, B. Leszczyńska-Madej, M. Madej, and M. Goły, "Microstructure and Mechanical Properties of Low-Cost SiC-Reinforced Aluminum and Al4Cu Matrix Composites Produced by Sintering in Vacuum," Materials, vol. 16, no. 15, article 5492, 2023, doi: https://doi.org/10.3390/ma16155492.
[11] F. Ahmad, V. B. Rajendren, X. Kai, S. U. Khan, S. S. A. Shah, R. Ullah, X. Chen, A. W. Zia, and Y. Zhao, "Effect of Y and Er microalloying on microstructure and corrosion behaviour of AA7085/Al2O3+ZrB2 composites," Journal of Materials Research and Technology, vol. 44, pp. 3792–3806, 2026, doi: https://doi.org/10.1016/j.jmrt.2026.08.241.
[12] D. A. Ashebir, G. A. Mengesha, and D. K. Sinha, "An insight into mechanical and metallurgical behavior of hybrid reinforced aluminum metal matrix composite," Advances in Materials Science and Engineering, vol. 2022, article 7843981, 2022, doi: https://doi.org/10.1155/2022/7843981.
[13] P. Morampudi, V. S. N. V. Ramana, V. S. P. Somayajula, S. Swetha, and K. A. Prabha, "Microstructural and mechanical characterization of Al6061-ZrB2 nanocomposites fabricated by powder metallurgy," Journal of the Mechanical Behavior of Materials, 2025, doi: https://doi.org/10.1515/jmbm-2024-0033.
[14] N. D. Vithal, B. B. Krishna, and M. G. Krishna, "Microstructure, mechanical properties and fracture mechanisms of ZrB_2 ceramic reinforced A7075 composites fabricated by stir casting," Materials Today Communications, article 101289, 2020, doi: https://doi.org/10.1016/j.mtcomm.2020.101289.
[15] E. A. Ananiadis, A. E. Karantzalis, A. K. Sfikas, E. Georgatis, and T. E. Matikas, "Aluminium Matrix Composites Reinforced with AlCrFeMnNi HEA Particulates: Microstructure, Mechanical and Corrosion Properties," Materials, vol. 16, no. 15, article 5491, 2023, doi: https://doi.org/10.3390/ma16155491.
[16] R. Cao et al., "Investigating the microstructure and performances of hot-extruded in situ ZrB_2/7085Al matrix composites," Materials Characterization, vol. 234, article 116223, 2026, doi: https://doi.org/10.1016/j.matchar.2026.116223.
[17] N. Muralidharan, K. Chockalingam, I. Dinaharan, and K. Kalaiselvan, "Microstructure and mechanical behavior of AA2024 aluminum matrix composites reinforced with in situ synthesized ZrB_2 particles," Journal of Alloys and Compounds, vol. 735, pp. 2167–2174, 2018, doi: https://doi.org/10.1016/j.jallcom.2017.11.371.
[18] Z. J. Wang, Z. Zheng, and M. W. Fu, "Aluminum matrix composites: Structural design and microstructure evolution in the deformation process," Journal of Materials Research and Technology, vol. 30, pp. 3724–3754, 2024, doi: https://doi.org/10.1016/j.jmrt.2024.03.237.
[19] A. J. Ansari, G. Bansal, and S. A. H. Rizvi, "Effect of reinforcement particles and multipass of friction stir processing on microstructure and mechanical properties of aluminium alloy," Materials Letters, vol. 355, article 135555, 2024, doi: https://doi.org/10.1016/j.matlet.2023.135555.
[20] Z. Chen, Z. Wu, H. Qian, Z. Wang, Q. Qiao, D. Guo, D. Zhang, C. T. Kwok, L. M. Tam, and X. Li, "Achieving synergistically enhanced corrosion resistance and hardness in nano-ZrB2/Al composites through friction stir based solid-state additive manufacturing," Corrosion Science, vol. 270, article 114011, 2026, doi: https://doi.org/10.1016/j.corsci.2026.114011.

*Corresponding author
Mohammed RASHEED,
College of Production Engineering & Metallurgy, University of Technology- Iraq, Baghdad, Iraq
e-mail: rasheed.mohammed40@yahoo.com

[21] M. Erol, Y. Bayrak, B. Özbay Kısasöz, M. A. Yılmaz, D. Özkan, and A. Kısasöz, "Unveiling the influence of CeO2 rare-earth oxide content on in-situ phase formation and properties of aluminium matrix composites," Ceramics International, 2025, doi: https://doi.org/10.1016/j.ceramint.2025.09.482.
[22] W. Long, J. Zhou, X. Hu, S. Liu, and W. Jiang, "Effect of In Situ Synthesized Al2O3 and TiC on the Microstructure and Properties of 6061 Aluminum Matrix Composites," Materials, 2026, doi: https://doi.org/10.3390/ma19020308.
[23] T. M. Gesing and L. Robben, "Determination of the average crystallite size and the crystallite size distribution: the envelope function approach EnvACS," Journal of Applied Crystallography, vol. 57, pp. 1466–1476, 2024, doi: https://doi.org/10.1107/S1600576724007362.
[24] I. Rosales-Cadena, R. A. Falcon-Castrejon, R. Guardian-Tapia, J. L. Roman-Zubillaga, S. R. Gonzaga-Segura, L. A. Falcon-Franco, V. H. Martinez-Landeros, and R. Servin, "The effect of ZrO_2 addition and thermal treatment on the microstructure and mechanical properties of aluminum metal matrix composites (AMMCs)," Materials, vol. 18, no. 19, article 4507, 2025, doi: https://doi.org/10.3390/ma18194507.
[25] N. Zhao, Z. Wang, X. Rong, D. Zhao, and C. He, "Advances in Interface of Powder Metallurgy Aluminum Matrix Composites Fabricated via In Situ Reaction: A Review," Acta Metallurgica Sinica, vol. 62, no. 5, pp. 923–940, 2026, doi: https://doi.org/10.11900/0412.1961.2025.00291.
[26] W. C. Oliver and G. M. Pharr, "Measurement of hardness and elastic modulus by instrumented indentation: Advances in understanding and refinements to methodology," Journal of Materials Research, vol. 19, no. 1, pp. 3–20, 2004, doi: https://doi.org/10.1557/JMR.2004.19.1.3.
[27] D. Zhang et al., "Mechanism of anisotropy elimination and synergistic enhancement of strength, ductility, and corrosion resistance by ZrB_2 in laser powder bed fusion fabricated aluminum composites," Journal of Alloys and Compounds, vol. 1079, article 190008, 2026, doi: https://doi.org/10.1016/j.jallcom.2026.190008.
[28] S. Sivakumar, B. R. Golla, and K. V. Rajulapati, "Influence of ZrB_2 hard ceramic reinforcement on mechanical and wear properties of aluminum," Ceramics International, vol. 45, pp. 7055–7070, 2019, doi: https://doi.org/10.1016/j.ceramint.2018.12.208.
[29] M. Ravikumar, R. Naik, R. Suresh, and K. Y. Chethana, "A Study of Mechanical and Wear Behavior of SiC-CeO2 Reinforced Al7075 Hot Rolled Hybrid Composites," Archives of Metallurgy and Materials, 2024, doi: https://doi.org/10.24425/amm.2024.150910.
[30] J. Yang, Y. Zhao, X. Kai, Y. Zhang, Y. Shan, and H. Zhu, "Synergistic enhancement of in-situ (Al2O3+ZrB2) nanoparticles and Er on microstructure and stress corrosion resistance of 7075Al matrix composites," Journal of Materials Research and Technology, vol. 36, pp. 6542–6554, 2025, doi: https://doi.org/10.1016/j.jmrt.2025.04.287.

*Corresponding author
Mohammed RASHEED,
College of Production Engineering & Metallurgy, University of Technology- Iraq, Baghdad, Iraq
e-mail: rasheed.mohammed40@yahoo.com